

SLAC – PUB – 4354

June 1987

I

## STATUS OF ČERENKOV RING IMAGING SYSTEMS\*

DAVID W.G.S. LEITH

*Stanford Linear Accelerator Center*

*Stanford University, Stanford, California, 94309*

### ABSTRACT

Čerenkov Ring Imaging is briefly introduced, and the problems or choices of designing such a counter are discussed. Recent results from the DELPHI and SLD prototype programs are presented and compared to the expected performance.

Invited talk given at the International Conference on  
Advances in Experimental Methods for Colliding Beam Physics,  
Stanford Linear Accelerator Center, Stanford  
March 9 – 13, 1987

---

\* Work supported by the Department of Energy, contract DE – AC03 – 76SF00515.

## 1. Introduction

In this review, I will explore the status of Čerenkov Ring Imaging Detectors. In section 1, I will briefly discuss what these new devices are, how they work, why we are interested in using them, and finally, who are working with such devices around the world. In section 2, I will look at the problems of principle in designing and building such devices, and in section 3 review the problems of practice in actually realizing a practical working device. I will then discuss the recent results from the prototype programs of DELPHI and SLD in section 4. Finally, I will draw some conclusions in section 5.

### 1.1 WHAT ARE RING IMAGING DEVICES?

Čerenkov Ring Imaging Detectors were proposed in 1977 by Ypsilantis and Seguinot [1] in an imaginative technical realization of an earlier idea of Roberts [2]. The new counters were not binary 'yes/no' devices, but offered good separation between all species of particles over a large dynamic range of momenta and promised to work well in the multiparticle jet environment of high energy collisions.

The principle behind these devices involves focussing the Čerenkov light emitted by a relativistic charged particle in passing through a radiator medium onto a high-efficiency photocathode, which can in turn be readout with good spatial resolution to localize the point of origin of the photoelectrons. This information permits the reconstruction of the circle of Čerenkov light for each particle above threshold, and hence the determination of the Čerenkov angle to an accuracy of a few percent. These principles are outlined in figs. 1(a)-(c).

## 1.2 HOW DO ČERENKOV RING IMAGING DEVICES WORK?

The mode of operation of such devices is shown schematically in figs. 2 and 3. A relativistic charged particle passing through the radiator material generates Čerenkov light at an angle to the particle's trajectory, given by the velocity of the particle and the index of refraction of the radiator material. [The angle,  $\theta = \arccos(1/\beta n)$ .] The light is emitted uniformly in azimuth around the particle direction. In our example in fig. 2, we show two radiators—a thin (1 cm) layer of liquid, and  $\sim 50$  cm of gas. The light from the liquid radiator is “proximity focussed” (i.e., is permitted to drift undisturbed) to the photon detector box. At a given azimuthal angle around the particle direction, the light from the gas radiator appears as a source at infinity to a spherical mirror so that a sharp ring image is focussed on a focal plane situated half the radius of curvature away from the mirror. In our case, we expect about two dozen photoelectrons from the 1 cm liquid radiator on a ring of about 17 cm radius and about 1 cm thickness, and about one dozen photoelectrons from the gas radiator around the circumference of a 3 cm radius ring which should be about 1 mm thick.

The Čerenkov photons are converted to electrons by photoionizing a complex organic gas molecule (tetrakis dimethylamino ethylene or more commonly called TMAE) which has a large photoionizing cross section in the (170-220) nm wavelength region. The TMAE gas is a 0.1% component of a regular drift gas mixture (e.g., 70% methane, 30% ethane) being flushed through the detector box—see fig. 3. The box has top and bottom windows of U.V. transmitting quartz, with sides of regular G-10 printed circuit board material. A uniform electric field along the axis of the detector box is provided by a double field cage—on the inside and outside surfaces of the box. The double cage prevents field inhomogeneities from local dielectric polarization. Typical drift fields are 400 V/cm. The Čerenkov photons entering the drift box convert to photoelectrons and the coordinates of the point of origin are recorded as the electron drift time, the wire address, and the conversion depth—as measured by a Multiwire Proportional Chamber

(MWPC) terminating the electron drift volume.

The three coordinate space-point information on each photoelectron allows the reconstruction of the Čerenkov circle image, and thereby a measurement of the Čerenkov angle.

### 1.3 WHY ARE CRIDS INTERESTING?

It is interesting to ask why we want particle identification when studying collisions involving 30 to 40 final state particles—what is the interest in knowing the identity of one or all? The answer has to do with how we tag or identify the basic constituents in the reactions—the quarks and gluons themselves. In fig. 4 we show how Ring Imaging Čerenkov information, together with good vertex information, can provide extremely clean (and rather efficient) tagging of heavy quark production in  $Z^0$  decays. The plot shows the mass spectrum for  $(K\pi\pi)$  combinations, from a Monte Carlo study of  $Z^0$  decays, with sequential use of the particle identification tools in SLD [3]. The results are from a study by Atwood [4].

### 1.4 WHO ARE WORKING ON RING IMAGING DEVICES?

There are four groups actively working on Čerenkov Ring Imaging systems these days—two on fixed target experiments, providing limited solid angle coverage, but giving  $\pi$ ,  $K$ ,  $p$  separation up to momenta of hundreds of GeV/c, and two  $4\pi$  colliding beam experiments. We describe each effort briefly below.

- E-605:

An experiment using the external (400-800) GeV/c proton beam at FNAL where the Čerenkov counter was used to provide  $\pi/K/p$  identification for the secondary particles up to  $\sim 200$  GeV/c [5]. This experiment took data in 1984.

- Omega Spectrometer:

A Rutherford Laboratory group designed and built a Čerenkov counter to study forward produced hadrons in 140 GeV/c  $\pi^+p$  and (70-200) GeV/c  $\gamma p$  interactions [6]. They took data in 1985 and 1986.

- 4 $\pi$  Detectors

The DELPHI [7] and SLD [3] experiments proposing to study  $Z^0$  decays at the LEP and SLC colliders both include Čerenkov Ring Imaging Devices to identify  $e$ ,  $\pi$ ,  $K$ ,  $p$  in the (1/2 – 50) GeV/c range. Both experiments hope to take data in the 1989 to 1990 time period.

## 2. Problems of Principle

Below I list the problems of *principle* which have to be faced in designing a Čerenkov Ring Imaging Detector, and continue to briefly discuss a selection of them for the remainder of this section:

- choice of radiator,
- choice of photocathode,
- optics scheme,
- electron detection,
- photon feedback protection,
- third coordinate readout scheme.

### 2.1 CHOICE OF RADIATOR

When choosing the gas or liquid to be the Čerenkov radiator, one must satisfy the following criteria:

- (a) It should be transparent to light in the wavelength window of the photocathode.

- (b) The index of refraction of the medium should be appropriate for the  $\gamma$  range being studied in the experiment. (Note that  $\gamma_{\text{th}} = \frac{1}{\sqrt{(1-1/n^2)}}$  and particle separation works fairly well up to  $\gamma \sim 7\gamma_{\text{th}}$  for a given radiator.)
- (c) There should be no nasty chromatic effects for the radiator material within the wavelength range to be used, (e.g., no absorption bands).

Table I gives the radiator choices of the four groups working with practical detectors, along with the intended momentum range for particle identification and an indication of how well their radiator/photocathode choices had worked out.

In fig. 5(a) the measured radius for  $\pi$ ,  $K$  and  $p$  as a function of momentum is shown for the FNAL experiment, E-605. Figure 5(b) shows the fitted radius for tracks of 200 GeV/c momentum. It shows a width of  $\sigma = 0.71$  mm for a Čerenkov circle of radius 70 mm!

Figure 6 shows the expected performance for the CERN-RAL experiment. Figure 7 shows the expected performance for the DELPHI and SLD experiments.

## 2.2 CHOICE OF PHOTOCATHODE

In the early days of exploring the Čerenkov Ring Imaging Detector (CRID) technology, many different "photocathode" materials were explored. A summary of potential candidates is given in fig. 8 and described in refs. [1, 8].

In recent years only two photoionizing gases have been broadly used. They are triethylamine or TEA, and tetrakis dimethylamine ethylene, otherwise known as TMAE. Their properties are listed and contrasted in table II.

TMAE is now the photocathode of choice given that it works well with readily available window material (viz. quartz) and that it forgives a few ppm contamination of oxygen or water vapor (rather than the ultra high purity demanded by TEA). The disadvantages of TMAE are its low vapor pressure and its effect on drift chamber lifetimes (see section 3.2 below).

### 2.3 ELECTRON DETECTION

One of the great challenges in the Čerenkov Ring Imaging technology is that the precious Čerenkov photon *signal* is characterized by the detection of a single electron, while most of the world's *noise* is similarly characterized. Efficiently detecting a single electron signal is not easy. Most of the usable drift chamber gases have an exponential pulse height distribution when run with reasonable gas gain ( $1 - 5 \times 10^5$ ) in the proportional region. A few gases (e.g., methane + quenching agent being one) have a Polya-like pulse height distribution for reasonable field values (see fig. 9). Such a pulse height distribution allows plateauing of the MWPC. The large dynamic range of pulse heights, coming from the fluctuations in the avalanche from the single parent, makes subsequent signal processing somewhat more awkward than for conventional tracking chambers.

### 2.4 PHOTON FEEDBACK

The positive feedback problem —photon feedback —is also a great nuisance and has to be faced head-on. The situation is schematically displayed in fig. 10, where a Čerenkov photon photoionizes a TMAE molecule in the Drift/Detector volume —the photoelectron drifts towards the MWPC anode under the action of a uniform electric field. At the anode surface the single, parent electron initiates an avalanche in the classic gas amplification process, is electrically recognized, and counted as detected. The chamber gas, left in an excited state by the avalanche process, de-excites optically allowing photons to stream back from the MWPC towards the “world's best photocathode,” the TMAE doped drift gas volume. The positive feedback process —the subsequent photoionization of the TMAE and reinitiation of more electron avalanches —is a disaster which must not be allowed to happen.

The general prescription for dealing with the photon feedback phenomena is:  
— shield neighboring anode wires so there is no direct illumination from wire-to-wire;

- limit the solid angle for photons backstreaming from the avalanche at an anode wire into the TMAE laden gas volume;
- since the light output from the avalanche grows exponentially as the chamber gain is increased beyond plateau, try to limit the gas gain to  $\sim (1 - 2) \times 10^5$ .

Let us examine several different implementations of these “rules.” The DELPHI detector solution is shown in fig. 11 [9]. Wire-to-wire isolation and the limiting of the back-streaming solid angle are achieved by 1 cm high alumina “blinds” inserted between each anode wire of their MWPC electron detector. The electric field to guide the photoelectrons to the amplifying fields at the anode surface is shaped by applying appropriate potentials to four conducting strips on the insulating blinds. They have had good experience with this structure.

For the SLD group, I show two recipes: one from the prototype detector, and another variation now under construction which is intended as our final solution [10]. In figs. 12 and 13, the wire-to-wire isolation is achieved by stretching the anodes in a u-shaped trench. The limiting of photon emission back into the TMAE volume is achieved by stringing fat (1 mm diameter) wires in a “cow-fence” arrangement. The potential of each fat wire is adjusted to give good (essentially 100%) collection of photoelectrons on the MWPC anodes. The final SLD detectors will have a similar construction, except the fat wires are replaced by 10 mil Be-Cu sheets, which have been etched to remove a 1 mm strip of metal directly in front of the anode (the anode pitch is 3 mm). The etched arrays are mounted into a monolithic package with good electrical and mechanical properties and substantially limit the solid angle for avalanche photons to find their way back to the TMAE volume.

Both the DELPHI and SLD proposals provide good cell-to-cell isolation, limit the photon feedback, allow for electrical termination of the drift field and have good, efficient electron detection.



## 2.5 THIRD COORDINATE READOUT

The third coordinate, or depth coordinate, readout is important to remove the parallax error from the measurement of the photoelectron point of origin. The Čerenkov photons are mostly *not* normal to the quartz windows as they enter the drift box and photoionize the TMAE. Furthermore, the absorption length of the Čerenkov light in the TMAE loaded drift gas is quite long (of order 20 mm). This leads to substantial connections to the point of origin measurement, as indicated in fig. 14.

The DELPHI solution is shown in fig. 15. Here we show again the alumina “blind” structure with the field shaping wires, and the 15  $\mu\text{m}$  gold plated tungsten anodes. The depth coordinate information is obtained by reading the signal induced (by the avalanche on the anode wire) on cathode strips. The strips are 5.4 mm wide and 42 mm long, and closely coupled (0.5 mm anode-to-cathode spacing) to 16 anode wires in a row. The pulse height on the cathode is  $\sim 30\%$  of that on the anode, and the avalanche signal typically spreads over three of the cathode strips for a single electron pulse. The DELPHI group have achieved  $\sigma \sim 2$  mm resolution for the depth measurement. The large signal developed by the energy loss from the passage of a charged particle represents a challenge for this readout method.

The SLD solution is to attempt charge division measurement at 1 – 2% accuracy for the 10 cm long anode wires. For this we use 7  $\mu\text{m}$  diameter carbon monofilaments for the MWPC anodes. These wires have a resistance of about 4000  $\Omega$  per cm. The carbon monofilaments have nice round cross sections with smooth surfaces and work well as anode wires. The typical breaking tension of a given fiber is (12-13) g, while the electrostatic stability criterion for the cell design requires  $\sim 0.5$  g tension. The chambers are strung with (4-6) g tension. Figure 16 shows the pulse height distribution as a  $\text{Fe}^{55}$  source was moved along a 10 cm carbon anode MWPC. The accuracy of the third coordinate measurement is shown in fig. 17, where averaged over all pulse heights a resolution  $\sigma_z = 1.7$

mm was achieved.

Table III summarizes the DELPHI and SLD solutions.

### 3. Problems of Practice

There are many choices to be made in the realization of a Čerenkov Ring Imaging Detector. I list below a representative sample of such choices, but due to pressure of time I will only discuss two items which I think are of special interest—viz. gas cleanliness and wire aging in a TMAE atmosphere.

Choices to be made:

- gas mixture,
- how to clean, and keep clean, the gases,
- operating temperature,
- gas seals,
- gas flow,
- implementation of electrostatics design,
- gating the MWPC,
- wire aging in a TMAE environment,
- calibration and monitoring.

#### 3.1 GAS PROBLEMS

The SLD group has had a very different experience with electron attenuation lengths in their prototype than has DELPHI. The CERN group began with electron attenuation length of (1.5 – 3.0) m, which grew to  $\sim 10$  m when they followed the treatment that the SLD group developed with Holroyd of washing the TMAE [11]. In contrast, at SLAC we had poor experience in the beginning (as demonstrated in fig. 18) which progressively improved with better understanding

of the gas system, of cleaning the TMAE liquid [11], of choice of construction materials, and of the passivation of surfaces in the gas lines and drift boxes. We now also have electron drift lengths of  $\sim 10$  m.

The washing of the commercial TMAE liquid provides a marked cleaning up of the extremely electronegative contaminants in the nominally clean TMAE as shown in fig. 19. Here gas chromatograph traces of TMAE from the chemist bottle is shown in (a), while that washed in distilled water and carefully dried is displayed in (b). The peaks labelled 1, 5 and 7 correspond to contamination of Dimethylene, Tetramethylurea and Tetramethyloxamide, which are all strongly electronegative molecules, and are substantially suppressed by the washing process.

### 3.2 WIRE AGING IN A TMAE ENVIRONMENT

Given that TMAE is such a good photo-absorber, it is natural to question how it behaves when repeatedly bathed in the light from the electron avalanche at the anodes of the MWPC. In other words, do chambers age differently with TMAE than with regular drift gas mixtures? The SLD CRID group has studied this issue for our chambers and found that they age much faster—showing factors of two loss in gain after radiation exposures producing  $10^{-4}$  C/cm along the anode wire compared to (0.1 – 1) C/cm for most drift chamber gases [12].

A 7  $\mu\text{m}$  diameter carbon fiber anode chamber was operated under regular conditions (6 l/hr. gas flow, methane plus TMAE (27°C) and the detector maintained at 45°C) with an  $\text{Fe}^{55}$  source radiating the anode. Figure 20 shows the drop in gain as a function of charge collected on the wire.

Now for serendipity! Figure 21 shows a series of “killings” of the chamber as in the previous case, but after each death we passed about 10 ma dc current through the resistive anode wires, raising their surface temperatures to 380°C and thereby removing the material causing the drop in gain. After about (10-20)

minutes of heating the chamber returns to full efficiency. The resistive anodes may be used to self-clean the chambers from the polymerization deposits [13].

The  $10^{-4}$  C/cm dose limit would allow the SLD CRID chambers to run for one to two years continuously, if the charge collection is dominated by the cosmic ray flux. Depending on the background conditions in SLC, the detectors may have to be regenerated once a year, or once every few months. The good news is that they can be regenerated!

## 4. Results from Prototype Tests of SLD and DELPHI

The SLD and DELPHI collaborations both have active prototype programs in which their respective detector elements are tested in a test beam environment. Their recent results are reported below.

### 4.1 THE DELPHI PROTOTYPE RESULTS

The DELPHI prototype is shown in fig. 22 and includes a full-sized liquid radiator tray, three full-sized drift boxes with detectors and a row of parabolic mirrors giving full coverage of one drift box. The vessel environment has been very carefully designed and controlled with regard to temperature and to high voltage; normal operating temperature was  $35^{\circ}\text{C}$ , and high voltages of over 100 kV can be maintained with a very uniform electric field in the region of the drift boxes. This system has been exercised in a 10 GeV/c pion beam at the CERN PS for over two years [9].

The drift gas used initially for their tests was a mixture of methane and isobutane (80 : 20) with typically 0.1% of TMAE. Later experiments used a methane/ethane mixture (75 : 25) for its better electron attenuation length characteristics. The radiators were perfluoro hexane- $\text{C}_6\text{F}_{14}$  for the 1 cm thick liquid radiator, and isobutane (later replaced by  $\text{C}_5\text{F}_{12}$ ) for the 45 cm of gas radiator. All of their gases were purified in one or two stages of an Oxisorb system and the

liquid was cleaned by closed circulation through an Oxisorb cartridge. Typically, there was less than 1 ppm of oxygen in the drift gas mixture.

Figure 23 shows a superposition of many beam tracks passing through the DELPHI prototype producing a liquid ring image spread over the three drift boxes, a large "beam spot" caused by the  $dE/dx$  energy loss of the 10 GeV/c pions passing through the drift box, and a small gas image ring. Typical single event images are shown in fig. 24. These are not the most recent, nor the best, images that this group has obtained. Their performance is summarized later in table IV. They have studied the effect of various angles of incidence for the charged track on the radiator. The liquid radiator image rapidly moves from a circle to an open ended parabolic figure as the angle of incidence moves away from normal due to internal reflection losses. This is shown in fig. 25 for both real data and for Monte Carlo simulation.

Data on how well they measure the Čerenkov angle for both liquid and gas radiators is shown in fig. 26, where (a) and (b) demonstrate the improvement in resolution when the third coordinate information from the cathode strips is used to remove the effects of parallax. In (c) and (d) the measurements are contrasted with the expectations from a Monte Carlo simulation.

Finally, the actual measured resolution for the Čerenkov angle is plotted for different incident angles and positions on the drift boxes and compared to the Monte Carlo estimate in fig. 27.

#### 4.2 THE SLD PROTOTYPE RESULTS

The ring imaging group in SLD has been testing a "proof-of-principle" prototype, designed to test most of the detector ideas in a full scale device but not in the specific geometry nor with the actual construction techniques to be used in the SLD CRID [10]. The prototype device is shown in fig. 28.

The prototype elements were mounted within an insulated aluminium box, 1 meter on each side, and maintained at a temperature of 40°C. The test devices

were:

- A liquid radiator cell which was all quartz construction, and part of a circulation system which pumped the  $C_6F_{14}$  radiator liquid through Oxisorb filters to remove oxygen and water vapor.
- A secondary electrostatic field cage wound with 1 mm diameter copper wire on a 2.5 cm pitch. This cage helped to maintain electric field uniformity in the drift box and to isolate the nearby electrical grounds.
- The drift box, which was 20 cm wide  $\times$  80 cm long  $\times$  4 cm deep at one end increasing to 6 cm at the detector end. The structure had G-10 printed circuit board sides and top and bottom UV transmitting quartz windows. A double field cage was wound on the inner and outer surfaces of the drift box with a 2.5 mm pitch which provided an adjustable uniform electric drift field in the range (50 – 600) V/cm.
- A spherical mirror with good ultraviolet reflectance ( $> 86\%$  in the region (1700-2200) Å) and adjustable such that the Čerenkov light produced in the 43 cm of gas radiator (isobutane for those tests) could be reflected back onto the drift box at any desired position along the length of the box.
- An electron detector to efficiently detect the single photoelectrons released from the TMAE photocathode. These electrons were detected by a picket fence of multi-wire proportional chambers working at a gain of  $(1 - 2) \times 10^5$ . In order to avoid a positive feedback situation, one has to limit the illumination of the TMAE volume by light emitted in the avalanche at the anodes of the MWPCs (see section 3.4 above). This was achieved in the prototype by using an array of thick copper wires, with graded electric field, to geometrically block the TMAE volume while maintaining full collection efficiency for the drifting electrons. The anodes were  $7 \mu\text{m}$  carbon monofilaments read out at both ends to provide the depth information (i.e. the third coordinate information) from measurement of the charge division.

Single event displays are shown in fig. 29 where (a) and (b) show 11 GeV/c  $\pi^+$  and  $K^+$  events, and (c), (d) show 4 GeV  $e^-$  and  $\pi^-$  events.

In fig. 30 the effect of the third coordinate information is dramatically displayed. In (a) the Čerenkov circle from the gas radiator, for 11 GeV  $\pi$ 's, is shown for about 200 events where only the time and wire number information are plotted. In (b), the data are corrected for the parallax error due to the varying depth of the photo conversion process inside the drift box. (Remember that the attenuation length for the Čerenkov light to photoionize the TMAE gas mixture is about 20 mm.) The Čerenkov circle is clearly observed to sharpen up after the correction. More quantitatively, the fitted radius distribution for the Čerenkov circles is shown for these two cases in fig. 31. A similar plot for the Čerenkov circle from the liquid radiator, with and without the third coordinate information, is shown in fig. 32.

Finally, the  $\pi/K$  separation capability is demonstrated in fig. 33, where the fitted ring radius of events is plotted for externally tagged  $\pi$ 's and  $K$ 's at 11 GeV/c. Extremely good separation is observed.

#### 4.3 SUMMARY

Table VI summarizes the results of these prototype programs. In general, the promises of the groups have been fulfilled in that the advertised electron yield and the accuracy of measurement of the Čerenkov angles have been achieved.

## 5. Conclusion

In summary, we should note that this new technology is making rapid advances. It has been successfully employed in two forward spectrometer experiments to provide particle identification in the momentum range (20-200) GeV/c [5-6]. Furthermore, the two  $4\pi$  devices in development for SLD and DELPHI have completed their proof-of-principle R&D with satisfactory results. Specifically, they report:

- the number of detected photoelectrons is as promised;
- long drift of single photoelectrons has been achieved routinely;
- the measurement resolution for the Čerenkov angle,  $\theta_C$ , is as promised;
- there are realistic solutions for the various construction and assembly issues.

To conclude, I think that the Čerenkov Ring Imaging Detector technology, began so adventurously ten years ago by J. Seguinot and T. Ypsilantis, has come along sufficiently well to be properly included in our repertoire of detection devices when designing and planning new experiments.



## REFERENCES

- [1] J. Seguinot and T. Ypsilantis, Nucl. Instr. and Meth. 142 (1977) 377.
- [2] A. Roberts, Nucl. Instr. and Meth. 9 (1960) 55.
- [3] SLD Design Report, SLAC-Report-273 (1984).
- [4] W. Atwood, private communication.
- [5] H. Glass et al., IEEE NS-32 (1985) 692; IEEE NS-30 1983 30.  
M. Adams et al., Nucl. Instr. and Meth. 217 (1983) 237.
- [6] R.J. Apsimon et al., IEEE NS-32 (1985) 674; and RAL Report 85-014.
- [7] DELPHI Proposal, LEPC 83-3, and LEPC 84-16.
- [8] A. Honma, S. Durkin, D. Leith, SLAC-PUB-2186 (1978).  
S. Williams, D. Leith, M. Poppe, T. Ypsilantis, IEEE NS-27 (1980) 91.
- [9] J. Seguinot, Second Hellenic School on Elementary Particle Physics (1985) 61.
- [10] V. Ashford, et al., Presented at the XXIII Intl. Conf. on High Energy Physics, Berkeley, CA, July 16-23, 1986; SLAC-PUB-4046.  
V. Ashford, et al., IEEE Trans. Nucl. Sci. NS-34 (1987) 499; SLAC-PUB-4118 (1986).
- [11] R. Holroyd, J. Preses, C. Woody, and R. Johnson, Presented at the XXIII Intl. Conf. on High Energy Physics, Berkeley, CA, July 16-23, 1986, CRID Internal Memorandum No. 18 (1986).
- [12] J. Va'Vra, IEEE Trans. Nucl. Sci. NS-34 (1987) 486; SLAC-PUB-4116 (1986).
- [13] J. Va'Vra private communication.

## FIGURE CAPTIONS

1. Schematic of Čerenkov counter operation; (a) a threshold counter, and (b) and (c) a Čerenkov Ring Imaging Detector.
2. A schematic of a two radiator Čerenkov Ring Imaging Detector.
3. Details of the electron drift box, which is the photon detecting component of a Čerenkov Ring Imaging Detector.
4. Mass distribution of  $K\pi\pi$  combination resulting from  $Z^0$  decays. (a) All appropriately charged combinations. (b) Identified  $\pi$  and  $K$  candidates using the CRID. (c) Three appropriate charged particles coming from a secondary vertex. (d) Identified  $\pi$ 's and  $K$ 's which come from a separated secondary vertex.
5. Results from the FNAL Experiment, E-605. (a) A schematic of the radius measurement for  $\pi$ ,  $K$ ,  $p$  as a function of momentum. (b) The measurement error for a sample of 200 GeV/c tracks.
6. The calculated performance of the Omega RICH.
7. The particle identification capability for a two radiator CRID, such as described in refs. [3, 7]. The performance of the liquid (FC-72) and gas (isobutane) radiators is shown separately. The dashed lines indicate the region where the heavier particle is below threshold. The separation is cut off at  $10\sigma$ , under the assumption that tails in measurement error distributions make it unrealistic to quote such large separations. The separation is shown for (a)  $e/\pi$ , (b)  $\pi/K$  and (c)  $K/p$ .
8. A summary of potential photocathode materials for ring imaging counters.
9. Typical pulse height distributions for single photoelectron detection in a MWPC. The solid line shows an exponential shape while the dotted line shows a Polya-like shape as seen in methane + quenching agent mixtures.
10. A schematic of the photon feedback phenomenon.

11. A schematic of the DELPHI RICH electron detector.
12. An electrostatic simulation of the SLD detector electron collection efficiency with a "cow fence" fat wire "blinding grid." A 6 kG axial magnetic field with a 200 G radial component is assumed in the calculation.
13. A schematic of the SLD CRID electron detector using an etched array "blinding grid."
14. A schematic display of the parallax error introduced in measurement of the point of origin of the photoelectron in a ring imaging counter.
15. The cathode strip readout scheme proposed by DELPHI RICH group.
16. Charge division spectra from a 10 cm long carbon fiber anode, as the  $\text{Fe}^{55}$  source is moved along the wire.
17. The charge division measurement for the 7  $\mu\text{m}$  diameter carbon monofilament SLD CRID chambers.
18. A schematic of electron drift attenuation measurements in SLD.
19. Gas chromatograph of (a) commercially available TMAE, and (b) TMAE washed with distilled water and carefully dried.
20. The loss of gain on the CRID MWPC as a function of radiation exposure measured as charge collected per cm of anode.
21. A series of "deaths" and "rejuvenations" of the CRID-MWPC, as the radiation exposure seriously reduces the chamber gain, and then heating of the carbon anodes by flowing a small dc current allows full efficiency to be regained.
22. The DELPHI RICH prototype.
23. The Čerenkov ring from many superimposed beam tracks passing through the 1 cm thick liquid radiator and the 45 cm gas radiator in the DELPHI RICH prototype.
24. Single event displays from the DELPHI RICH prototype.

25. The Čerenkov ring image from a steeply inclined track detected by the DELPHI RICH for (a) real data events in the prototype, and (b) the Monte Carlo simulation.
26. Measurement accuracy for the liquid and gas radiator in the DELPHI RICH showing effect of including third-coordinate readout.
27. Comparison of the measured and calculated Čerenkov angular resolution for both liquid and gas radiators in the DELPHI RICH.
28. Schematic of the proof-of-principle prototype of the CRID under test at SLAC.
29. Single event display from the SLD CRID; (a) and (b) are 11 GeV/c  $\pi^+$  and  $K^+$  respectively, while (c) and (d) are 4 GeV/c  $\pi^-$  and  $e^-$ , respectively.
30. (a) SLD Gas radiator Čerenkov ring images for multiple events with parallax unresolved, and (b) with parallax corrected with charge division depth coordinate information. Units in  $x$  and  $y$  axes are mm.
31. The radius distribution for the Čerenkov circles from the SLD prototype gas radiator is shown (a) with, and (b) without, the use of the charge division data to correct for parallax errors.
32. The distribution of Čerenkov angles for the circles from the liquid radiator of the SLD prototype is shown (a) with, and (b) without, the use of the charge division data to correct for parallax errors.
33. The Čerenkov ring radius from 11 GeV/c  $\pi^+$  and  $K^+$  in the gas radiator of the SLD prototype. Very clean separation is achieved.

Table I

Radiator Choices for Four Čerenkov Ring Imaging Detectors.

Radiator	$n$	$\gamma_{th}$	Pion Threshold (GeV/c)	Number of photoelectrons from $L_{cms}$ of Radiator	Experiment Goals
Helium	1.000038	116	16	(TEA) 6 from 1500 cms	E-605 $\pi, K, p$ (50-200) GeV/c
Nitrogen	1.00032	40	5.5	(TMAE) 28 from 500 cms	RAL-Omega $\pi, K, p$ (20-150) GeV/c
C <sub>5</sub> F <sub>12</sub>	1.0017	17	2.4	(TMAE) 12 from 45 cms	SLD/DELPHI $Z^0$ decays $e, \pi, K, p$ (1/2-40) GeV/c
C <sub>6</sub> F <sub>14</sub>	1.2176	1.5	0.2	(TMAE) 24 from 1 cm	

Table II

Comparison of TEA and TMAE Photocathodes

	TEA	TMAE
Absorption Length for Čerenkov Light	1 mm	(15-40) mm depending on temp.
High Edge of Wavelength Window	around 1500 Å	around 1950 Å
Requirement in O <sub>2</sub> , H <sub>2</sub> O	≤ 200 ppb	≤ 20 ppm
Window Material	CaF	Quartz

Table III

Comparison of DELPHI/RICH and SLD/CRID photoelectron detection schemes

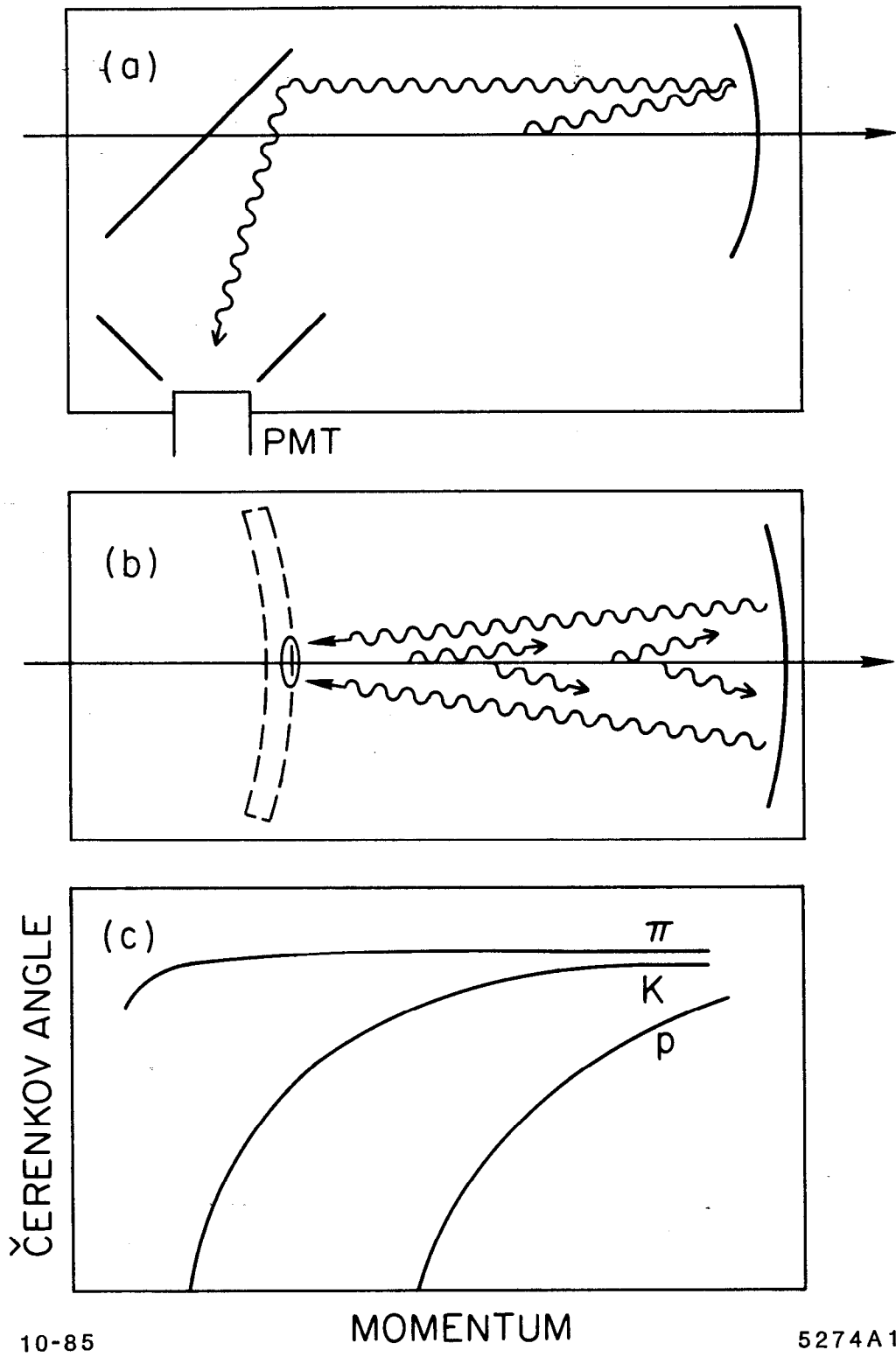
	DELPHI	SLD
Gas	80% CH <sub>4</sub> , 20% C <sub>2</sub> H <sub>6</sub> , 0.1% TMAE	Same
Gain	(1-2) × 10 <sup>5</sup>	Same
Blinding Structure	10 mm high alumina strips with 4 field shaping wires  Opening angle = 14°	Five layers of etched arrays with tapered $\vec{E}$ field  = 6.6°
Anode	15 μ gold plated tungsten 2.6 mm spacing	7 μ carbon 3.1 mm spacing
Anode-to-Cathode Space	0.5 mm	1.6 mm
Third Coordinate Readout	Cathode Strips 5.4 mm high x 42 mm long 30% of anode signal 3 strips hit for 1 p.e. $\sigma_z \sim 2$ mm $E_c \sim 85\%$ at beginning of plateau	Resistive wires and charge division  $\sigma_z \sim 1.5$ mm

Table IV

Summary of the Results of the DELPHI/RICH and SLD/CRID Prototype Programs

Experiment	Radiator	Photocathode	Number of Photoelectrons		$\sigma(\theta)$ per p.e. (mrad)	$\theta + \delta\theta$ (mrad)
			Detected	Expected		
E-605 (FNAL)	1500 cm He	TEA	3	6	$\pm 0.2$	$8.7 \pm 0.09$
RAL-OMEGA (CERN)	500 cm N <sub>2</sub>	TMAE	12	28	$\pm 0.5$	$25.8 \pm 0.14$
SLD (SLAC)	43 cm Isobutane	TMAE	11.5	12	$\pm 4.3$	$56.4 \pm 1.2$
	1 cm C <sub>6</sub> F <sub>12</sub>	TMAE	$\sim 34$	24	$\pm 16$	$668 \pm 2.6$
DELPHI (CERN)	48 cm Isobutane	TMAE	10	12	$\pm 4.5$	$53.7 \pm 1.4$
	48 cm C <sub>5</sub> F <sub>12</sub>	TMAE	13	16	$\pm 4.5$	$56.9 \pm 1.2$
	1 cm C <sub>6</sub> F <sub>14</sub>	TMAE	21.5	24	$\pm(12 - 17)$	$680 \pm 2.4$





10-85

MOMENTUM

5274A1

Fig. 1

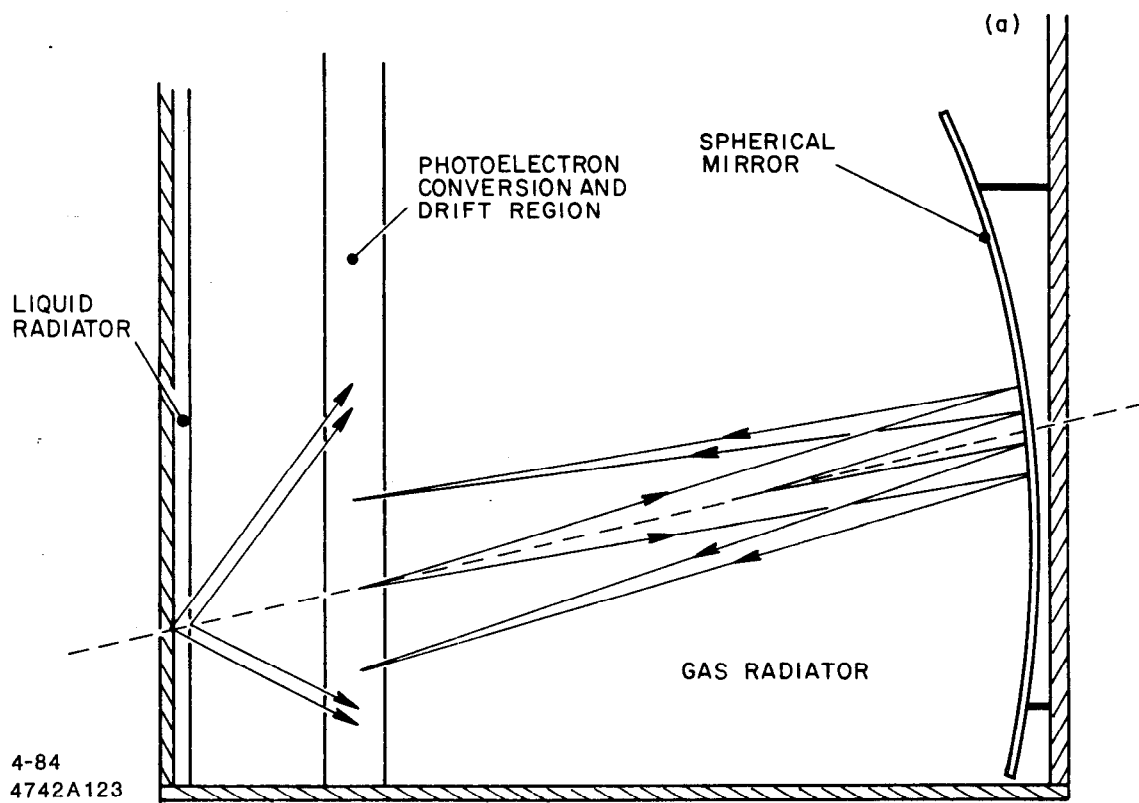


Fig. 2

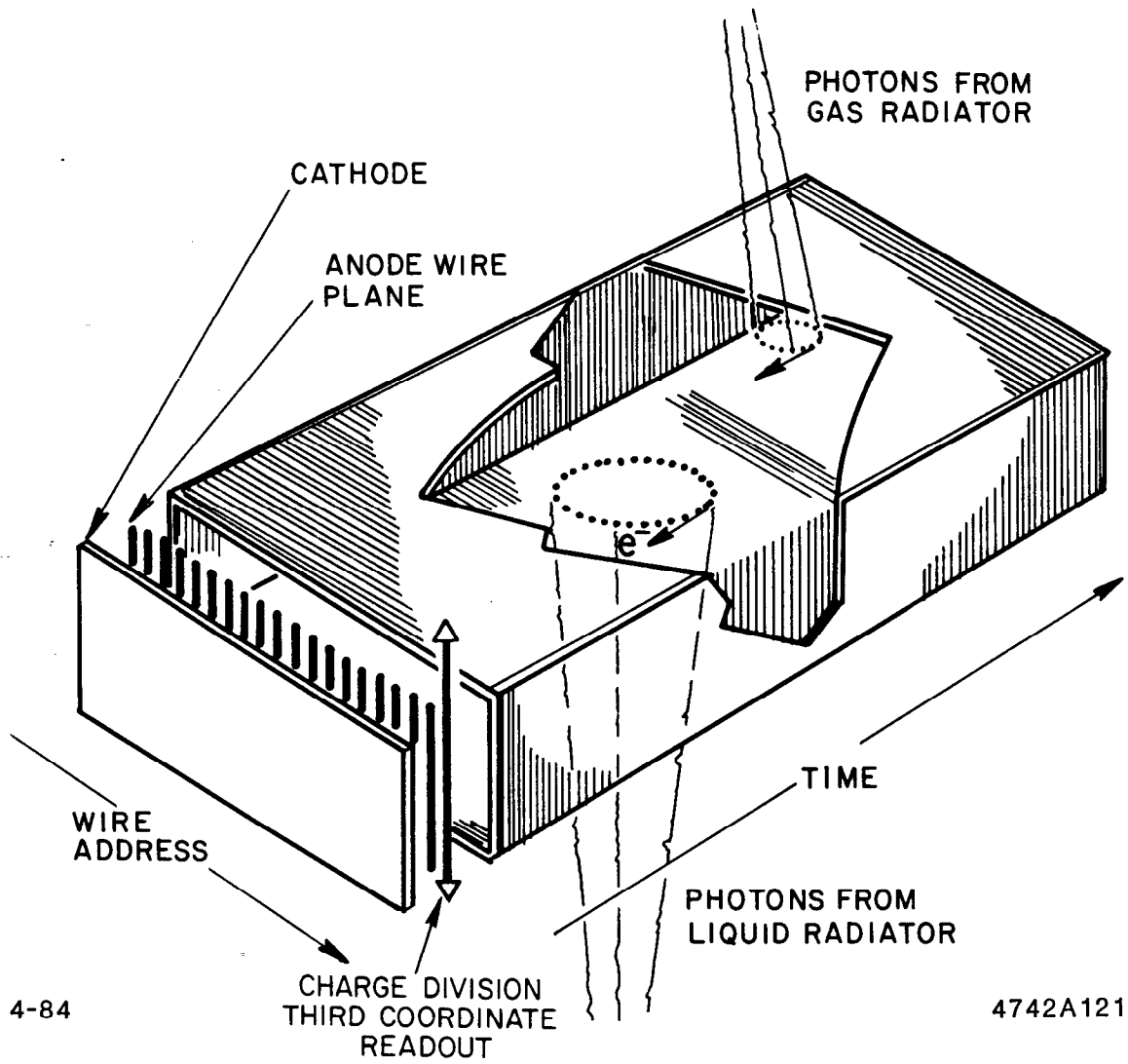


Fig. 3

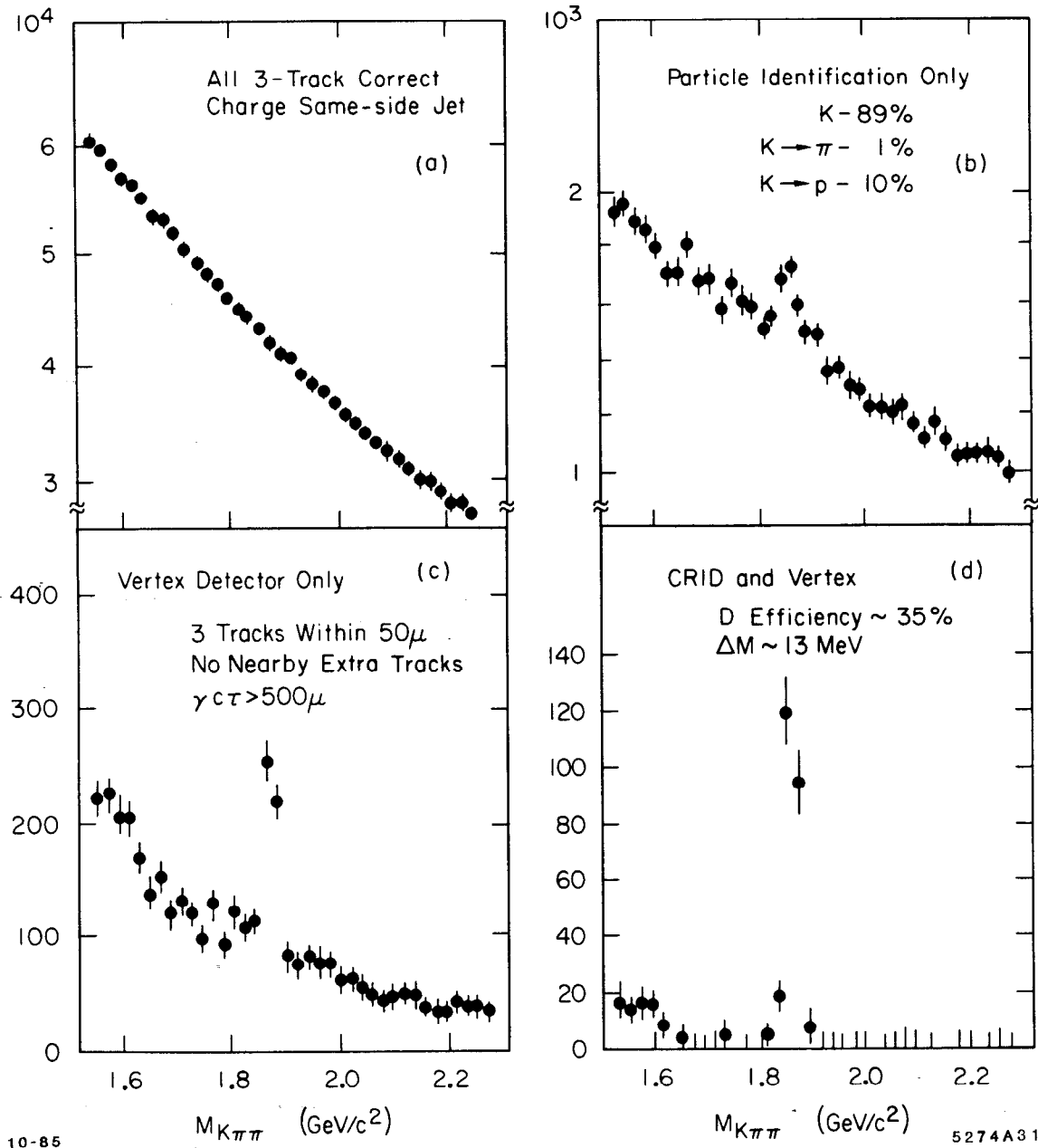
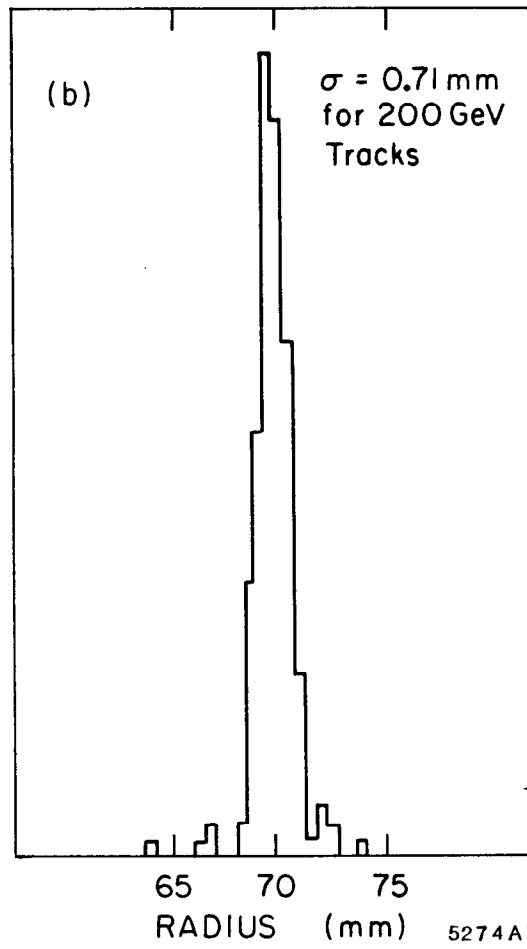
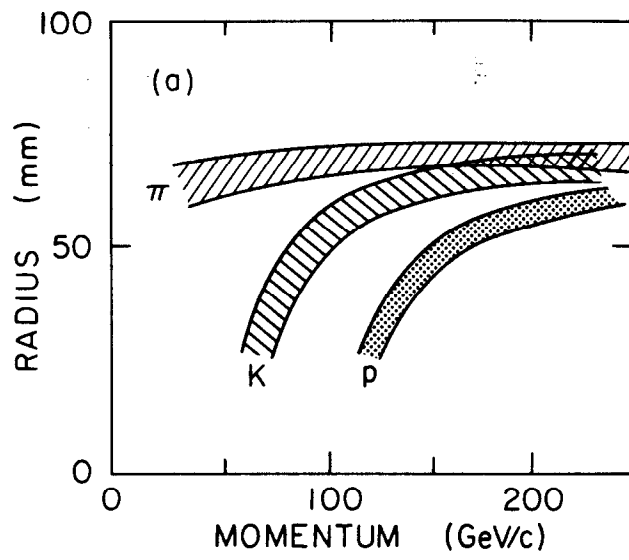


Fig. 4



10-85

5274A7

Fig. 5

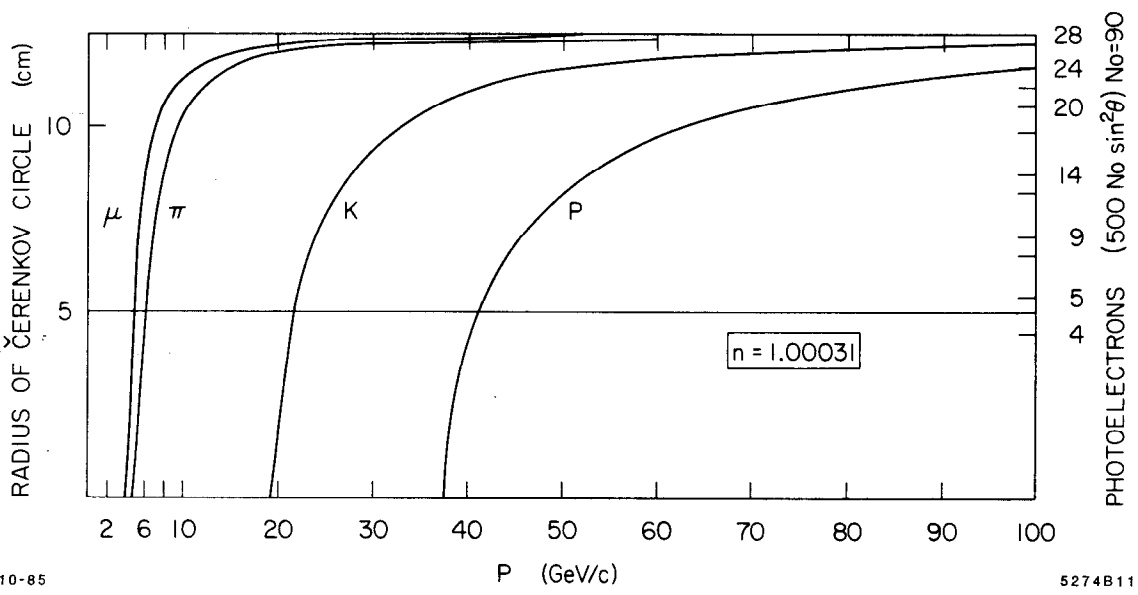


Fig. 6

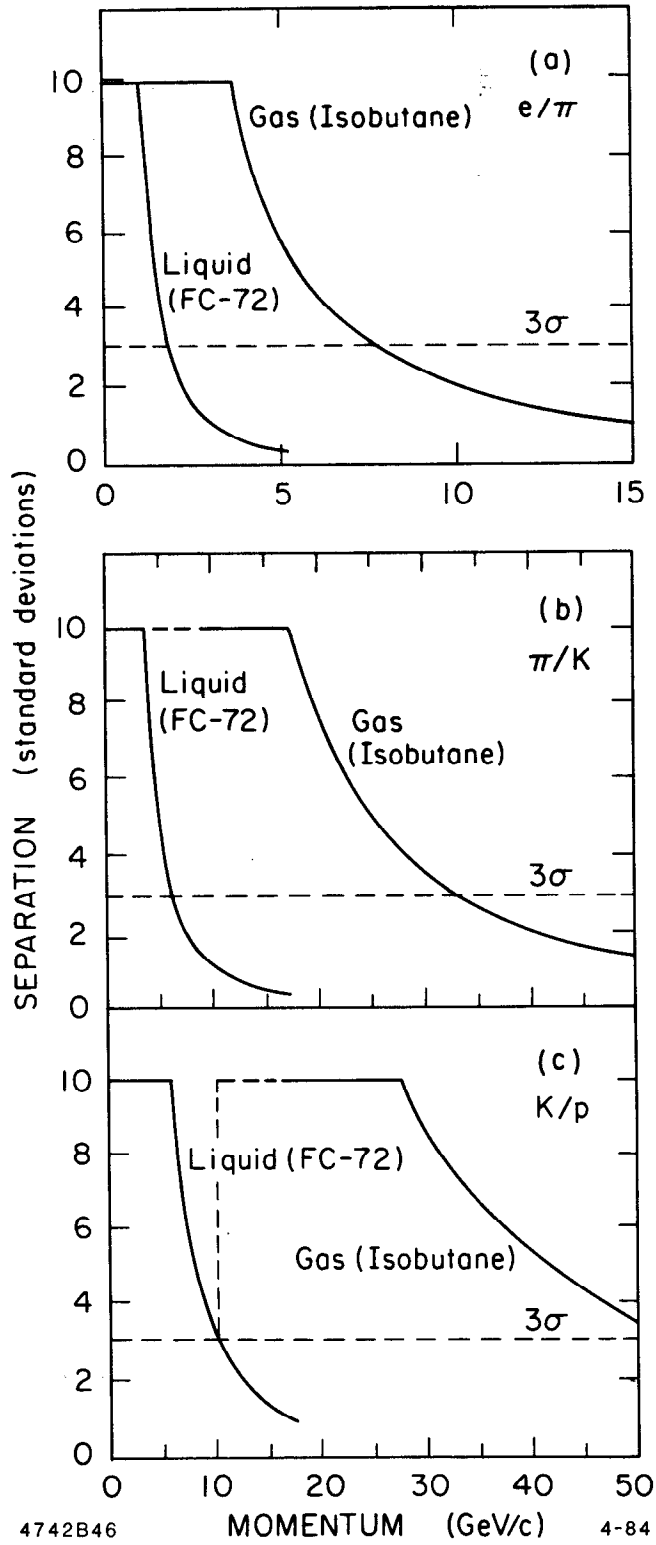


Fig. 7

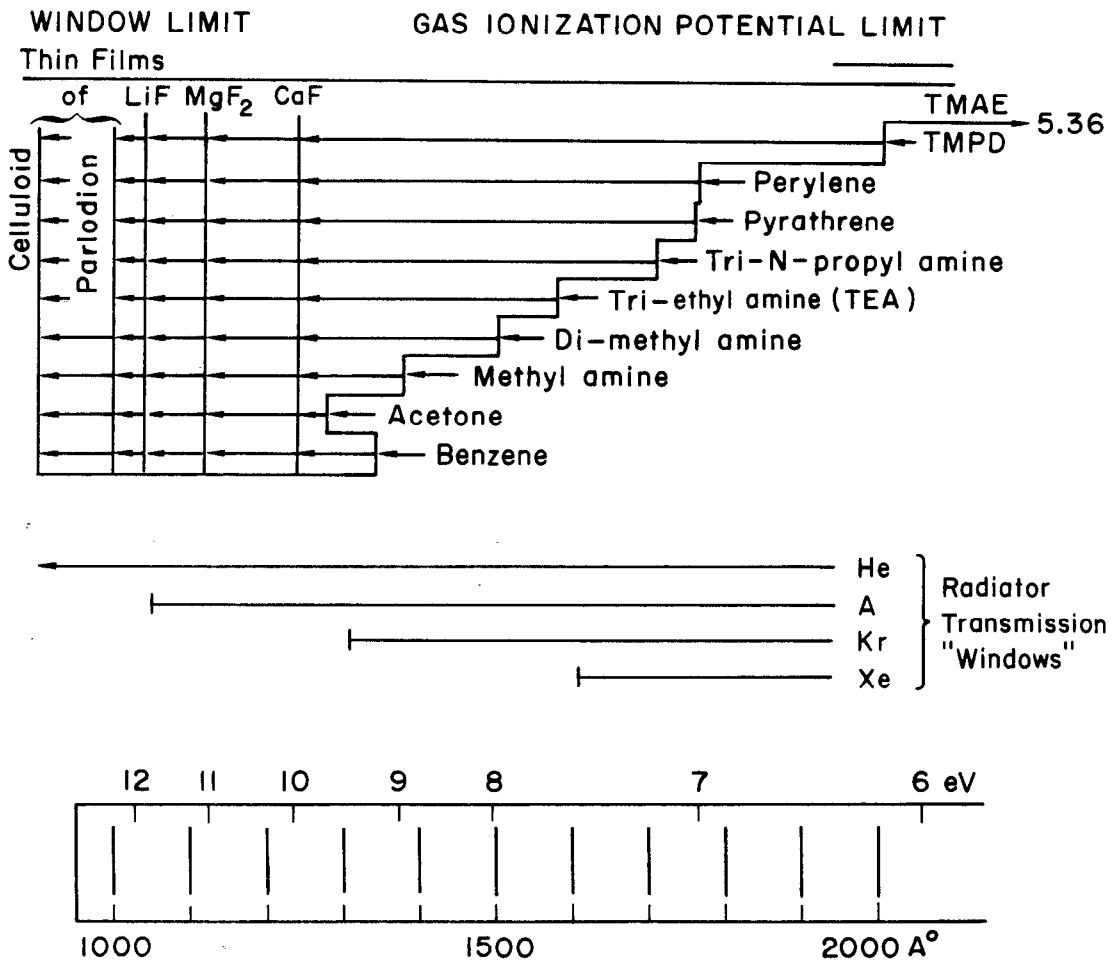


Fig. 8



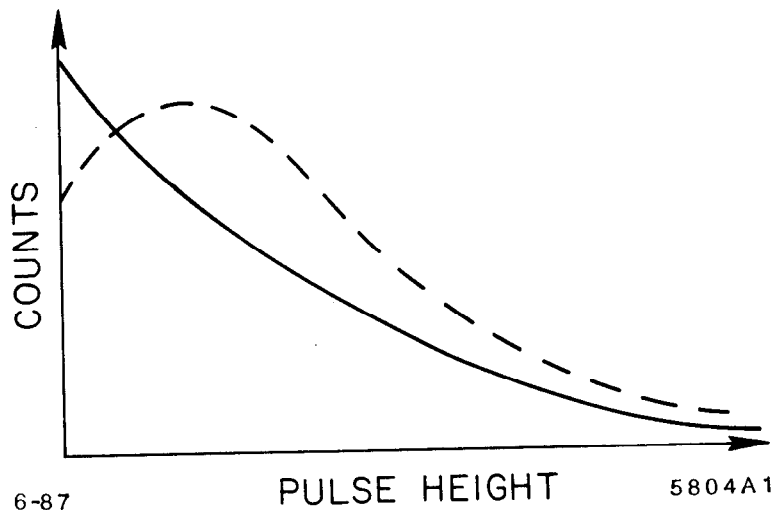
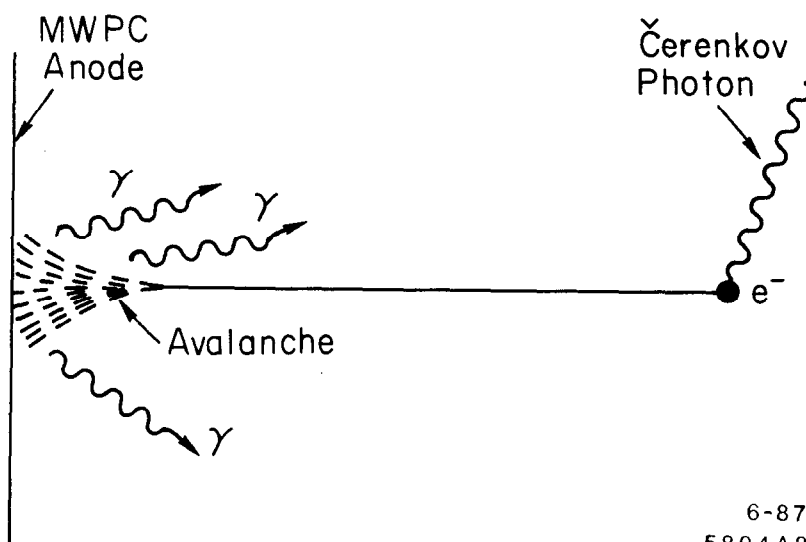


Fig. 9



6-87  
5804A2

Fig. 10

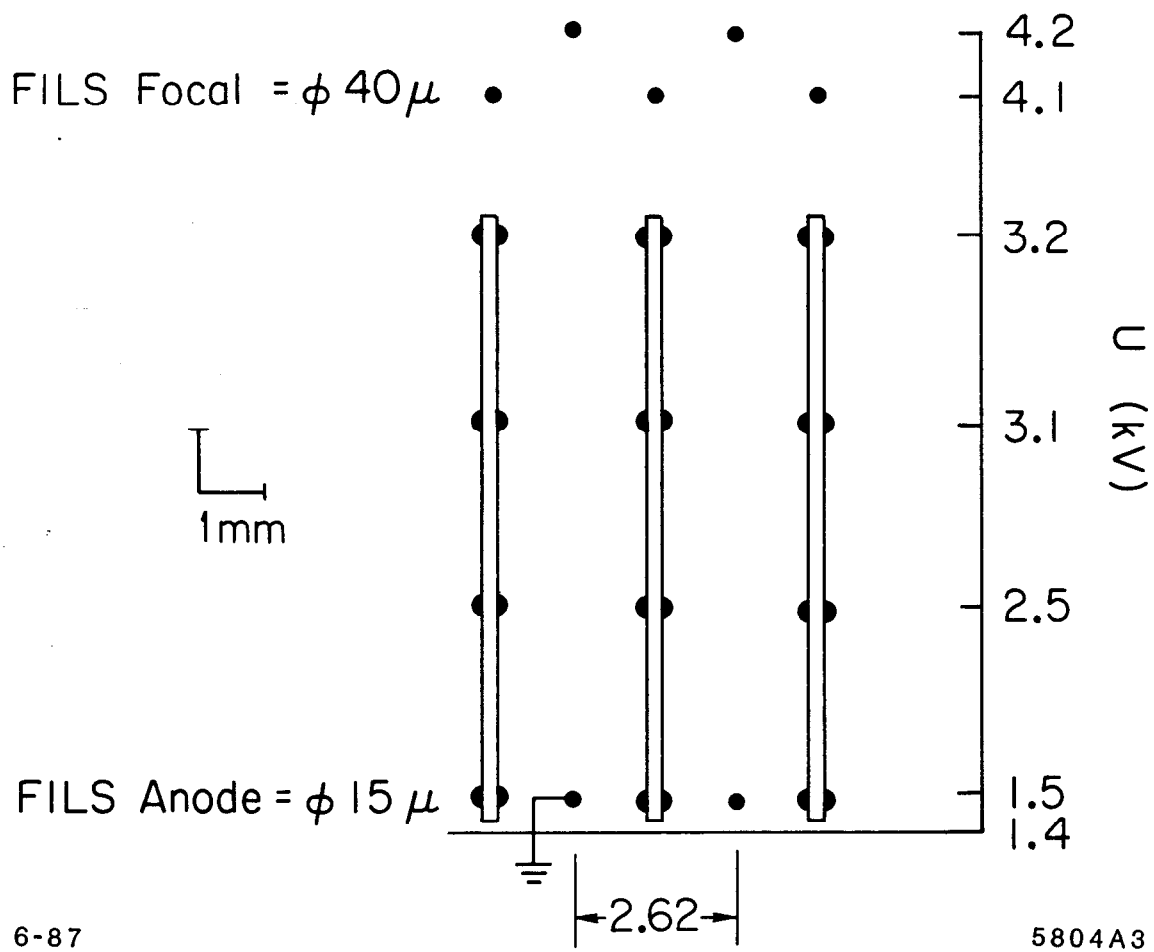
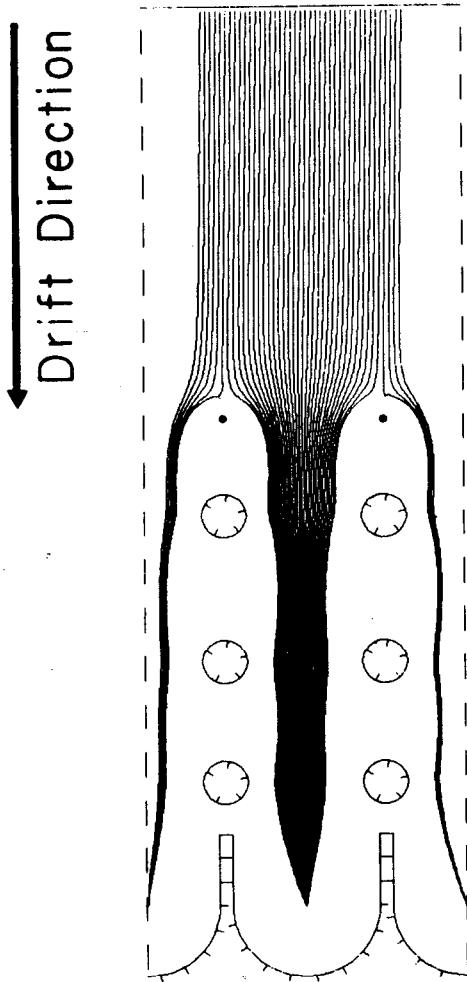


Fig. 11



B Field: 0.0 6.0 0.2 kG

Mobility:  
 $7.5 \text{ cm}^2 / (\text{kV microsec})$

Drift Field: 500 V/cm

Guide Wires: -3.70 kV

Voltage: -3.30 kV

Voltage: -2.70 kV

Blind Wires: -2.20 kV

Radius: 450.0 microns

Anode Voltage: 0 kV

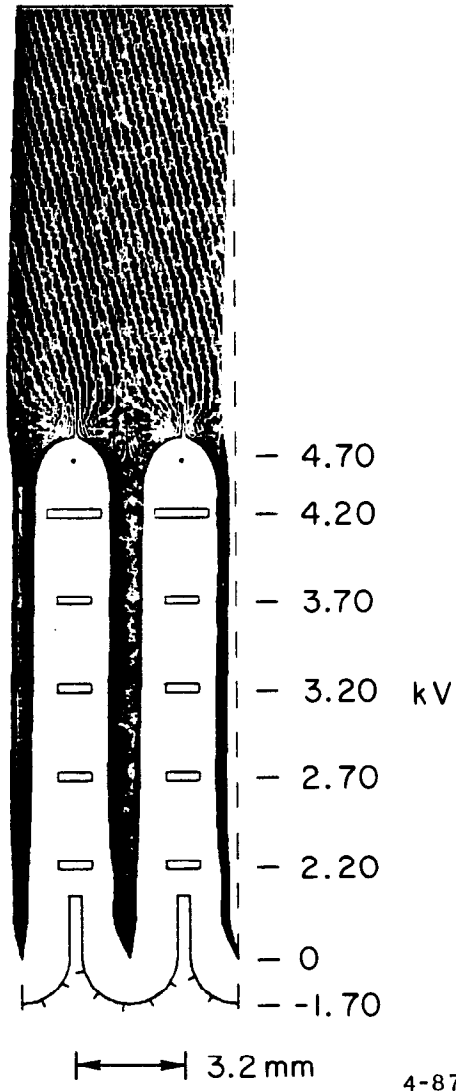
Cathode Voltage: -2.00 kV

10-85

5257A1

Fig. 12

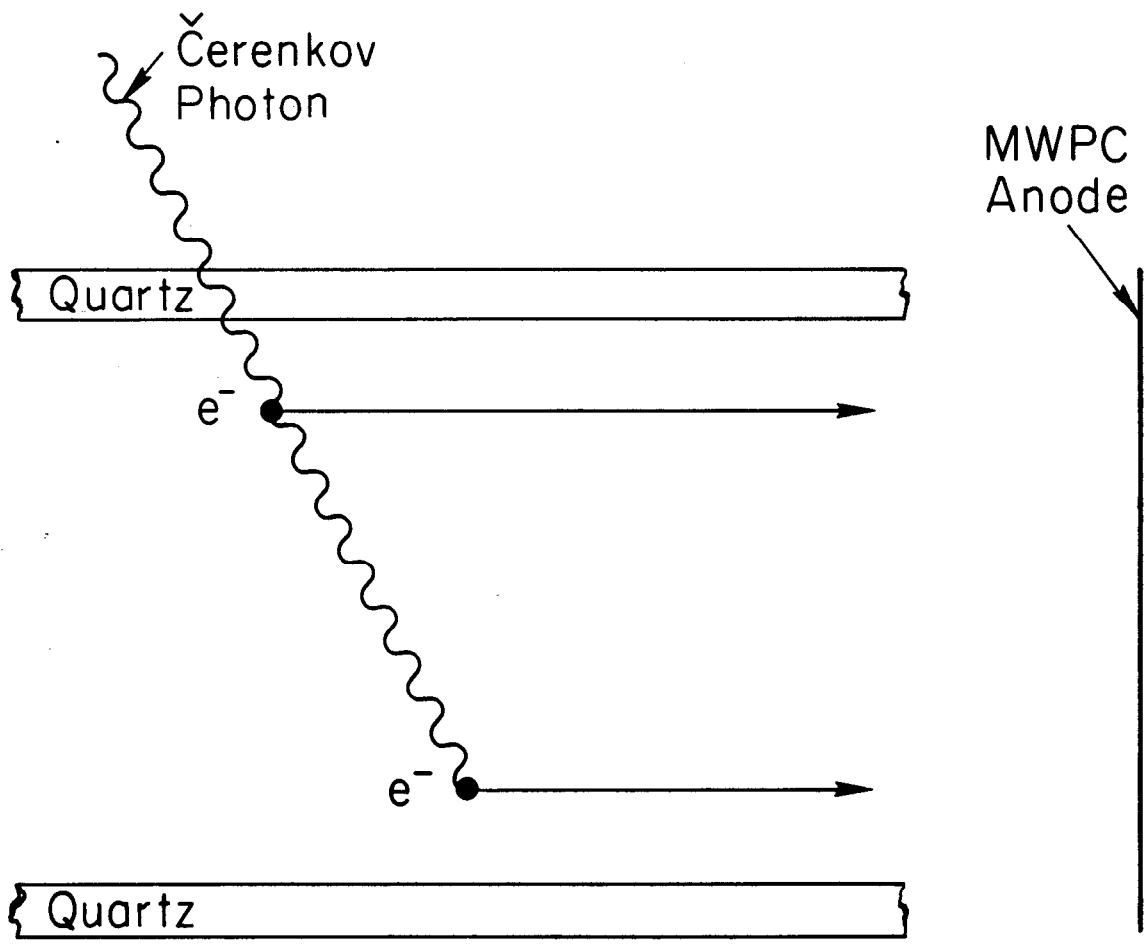
400 V/cm  
Drift



5708A10

4-87

Fig. 13



6-87

5804A4

Fig. 14

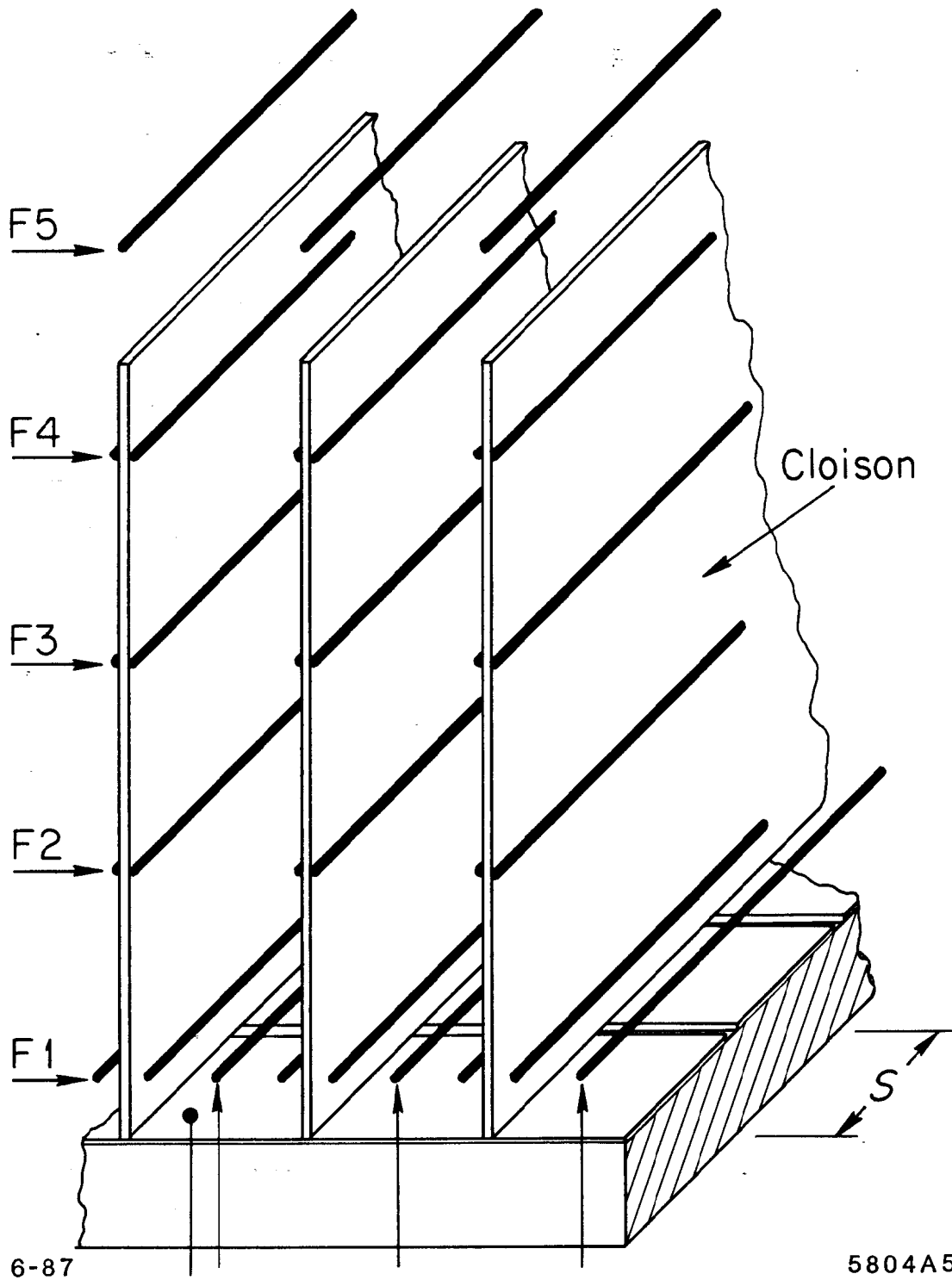
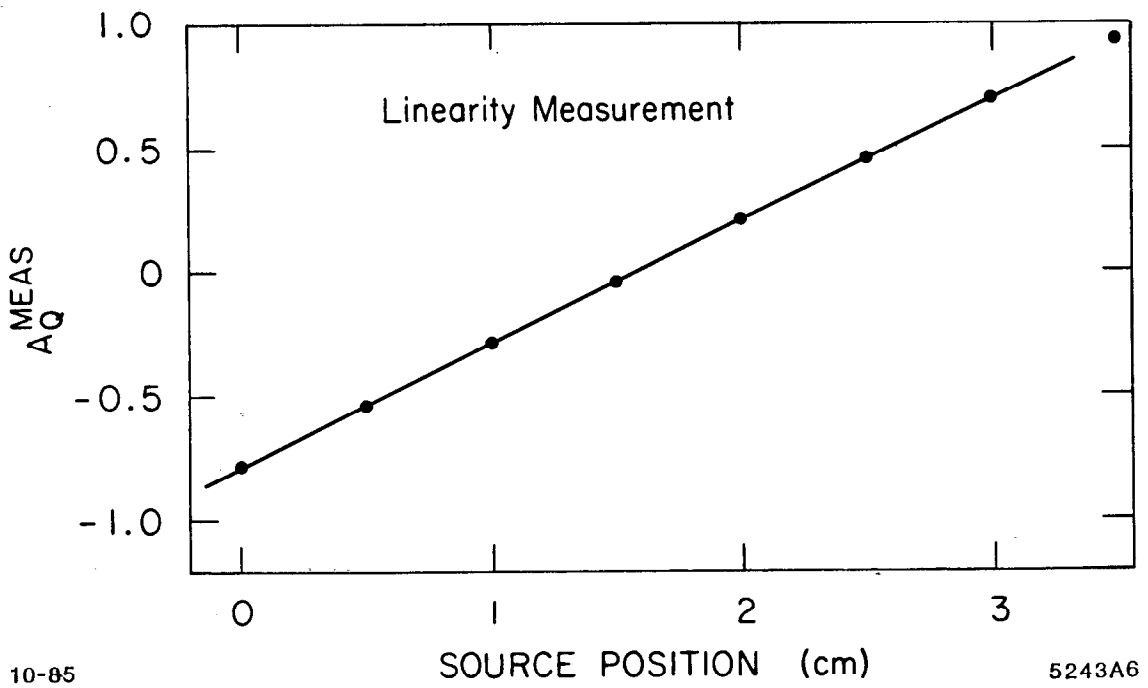
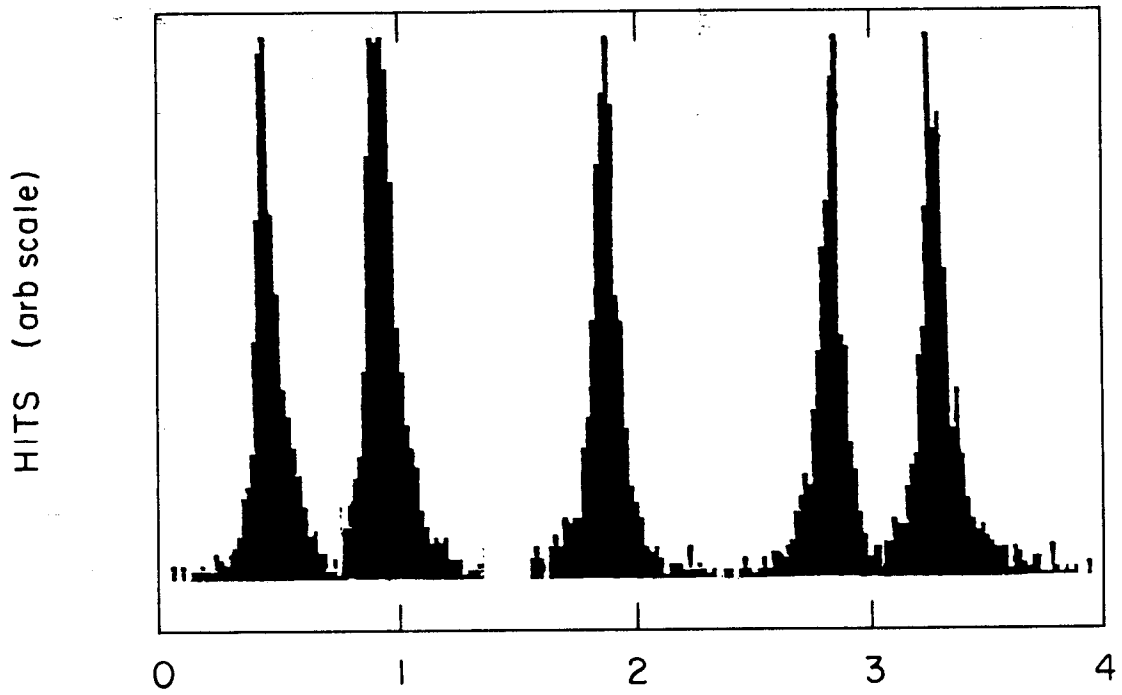


Fig. 15



10-85

5243A6

Fig. 16



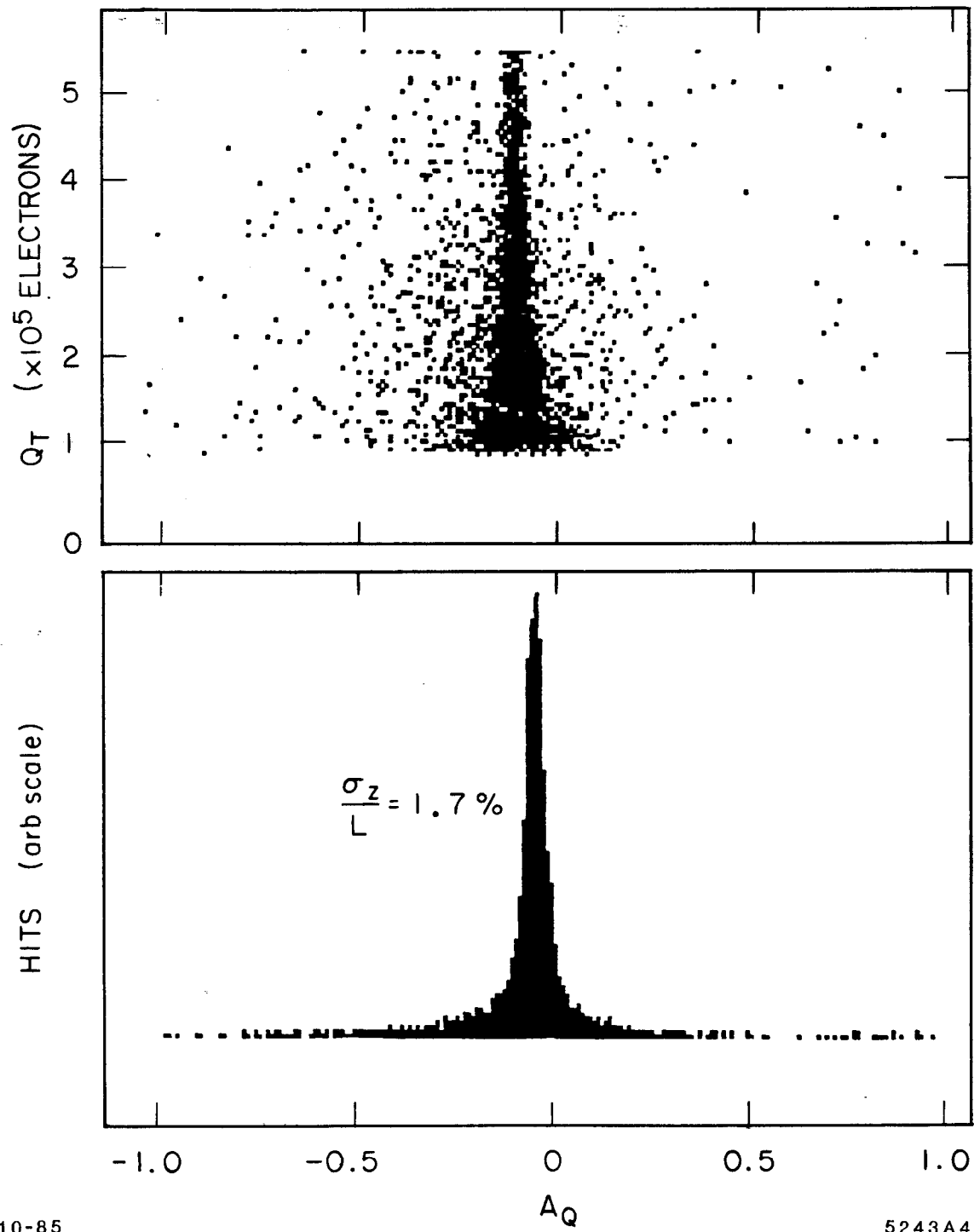


Fig. 17

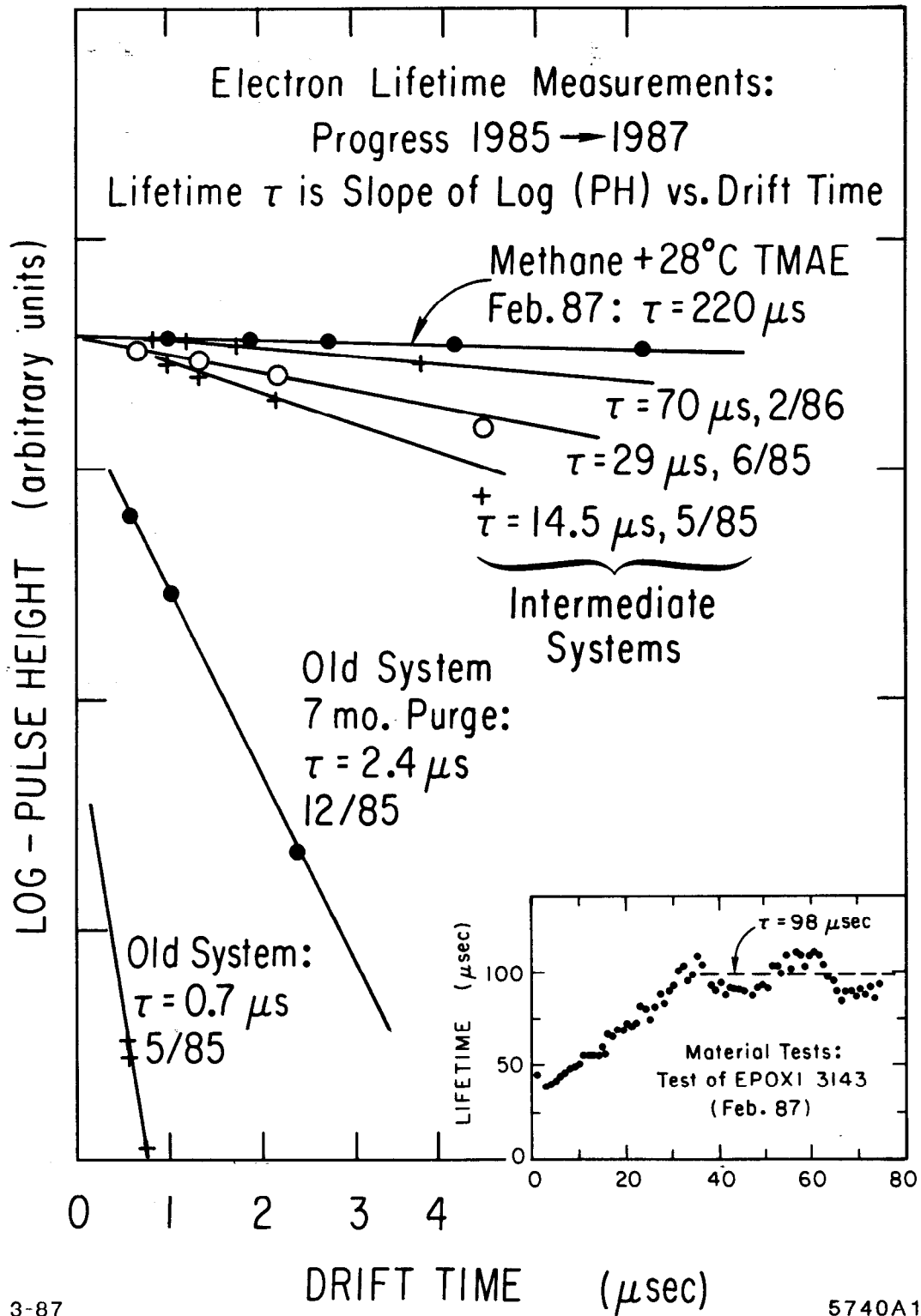
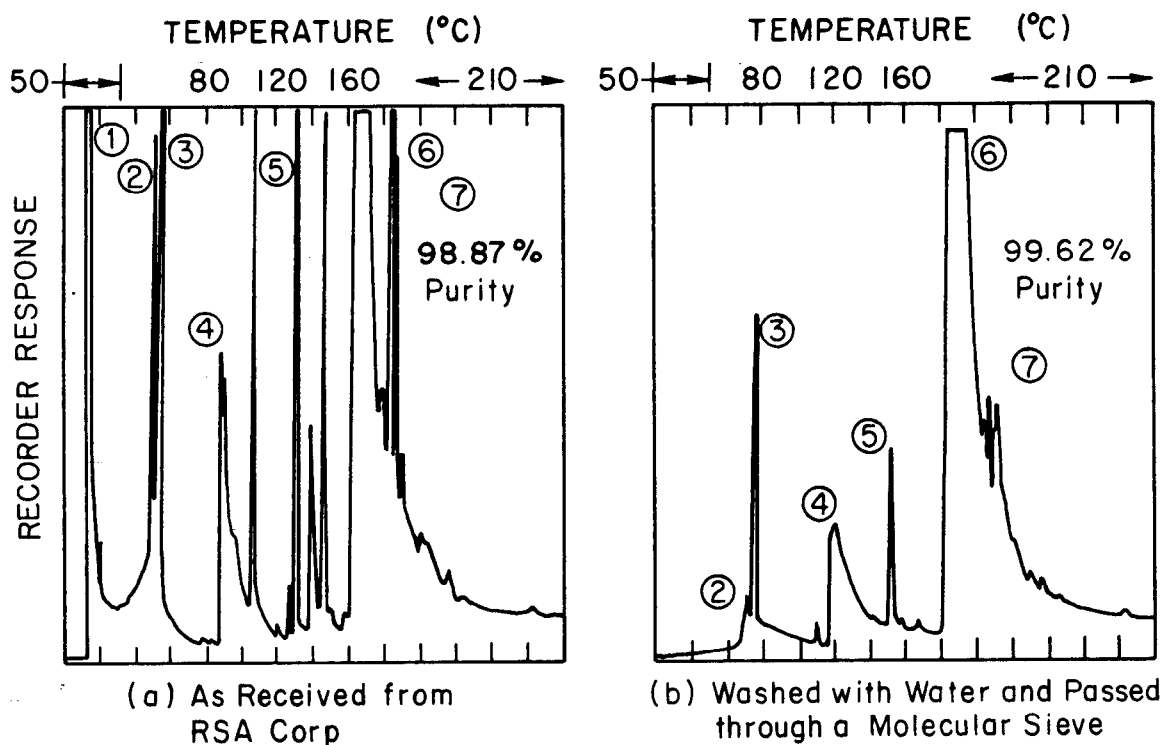


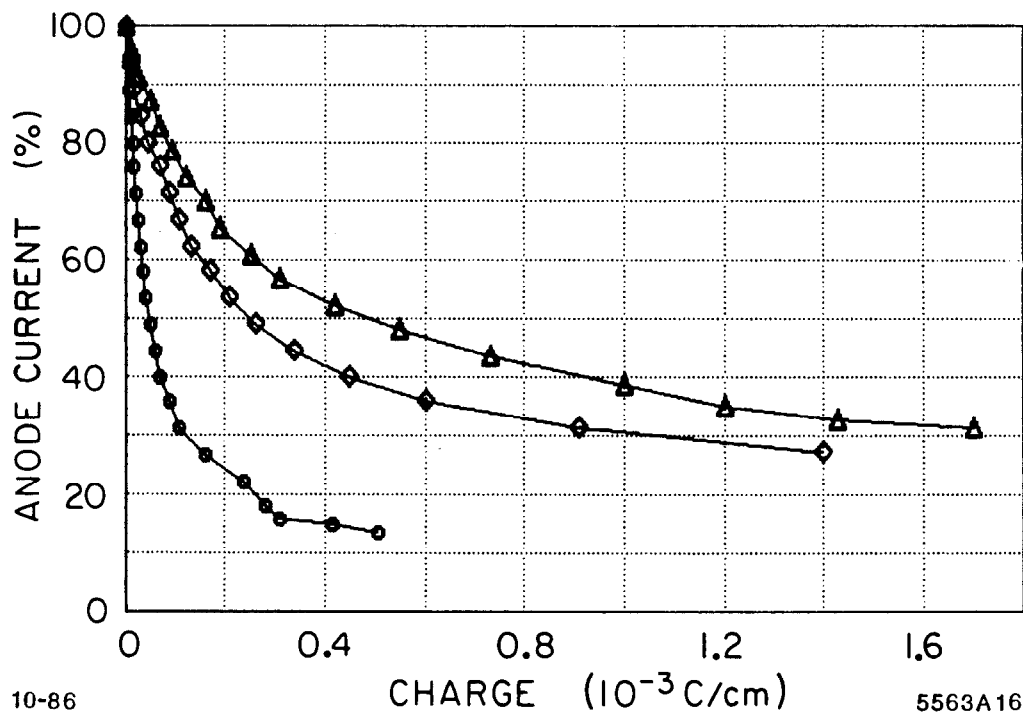
Fig. 18



#### Symbol Identification

Symbol	Name	Formula	MW
DMA	Dimethylamine	$(\text{CH}_3)_2\text{NH}$	45
TMH	Tetramethylhydrazine	$(\text{CH}_3)_2 - \text{N} - \text{N}(\text{CH}_3)_2$	88
BMAM	Bis(dimethylamino)methane	$[(\text{CH}_3)_2\text{N}]_2 - \text{CH}_2$	102
DMF	Dimethylformamide	$\text{H}(\text{C} = \text{O}) - \text{N}(\text{CH}_3)_2$	73
TMU	Tetramethylurea	$[(\text{CH}_3)_2\text{N}]_2 - \text{C} = \text{O}$	116
TMAE	Tetrakis(dimethylamino)ethylene	$\text{C}_2[(\text{CH}_3)_2\text{N}]_4$	200
TMO	Tetramethyloxamide	$[(\text{CH}_3)_2\text{N}]_2 - (\text{C} = \text{O})_2$	144

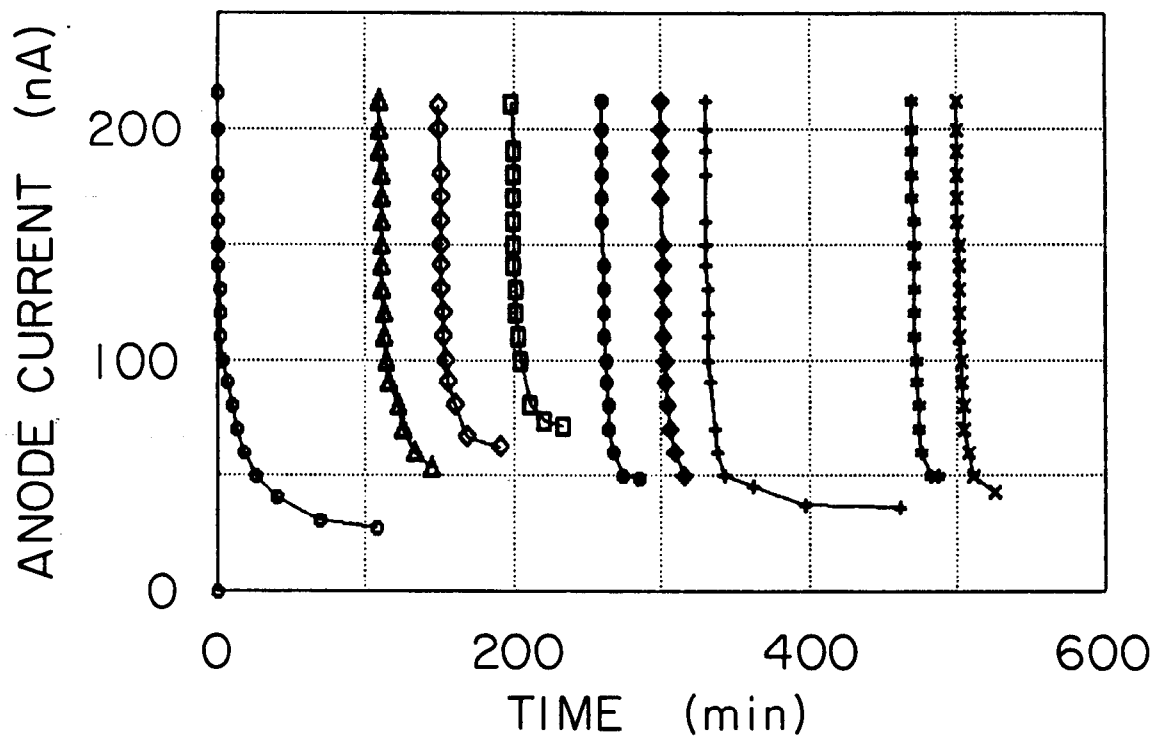
Fig. 19



10-86

5563A16

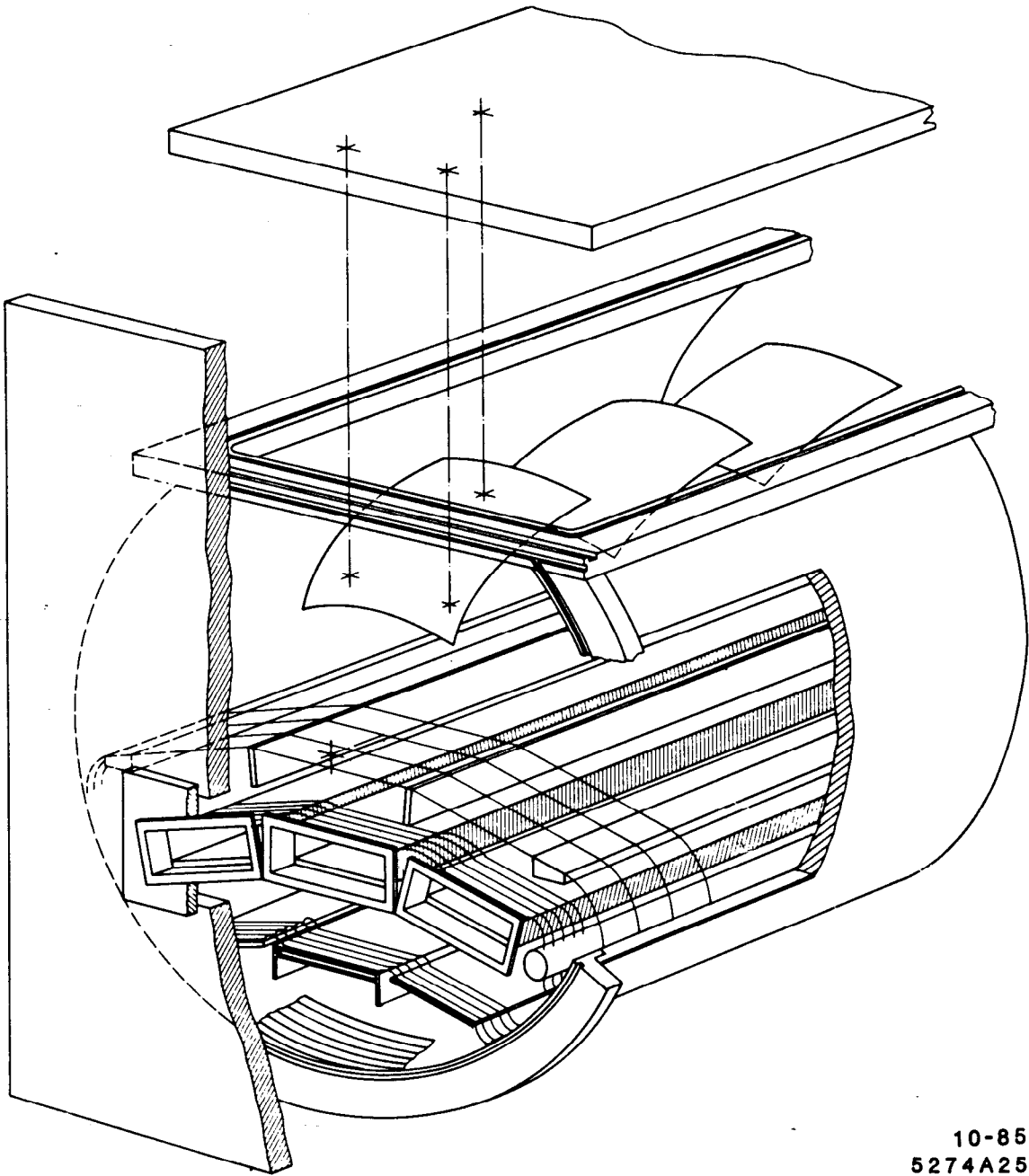
Fig. 20



6-87  
5804A6

(arbitrary offsets between measurement)

Fig. 21



10-85  
5274A25

Fig. 22

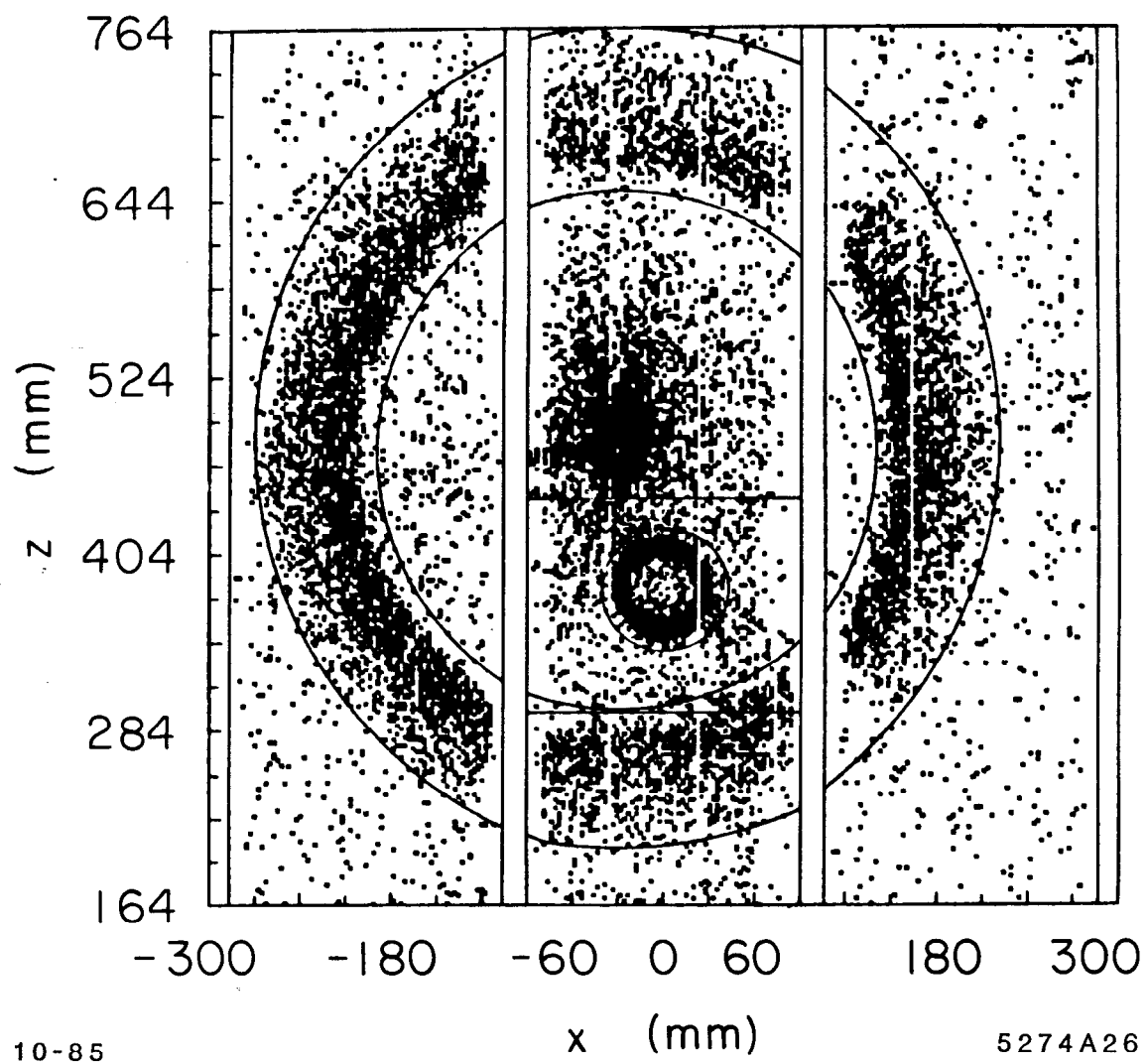
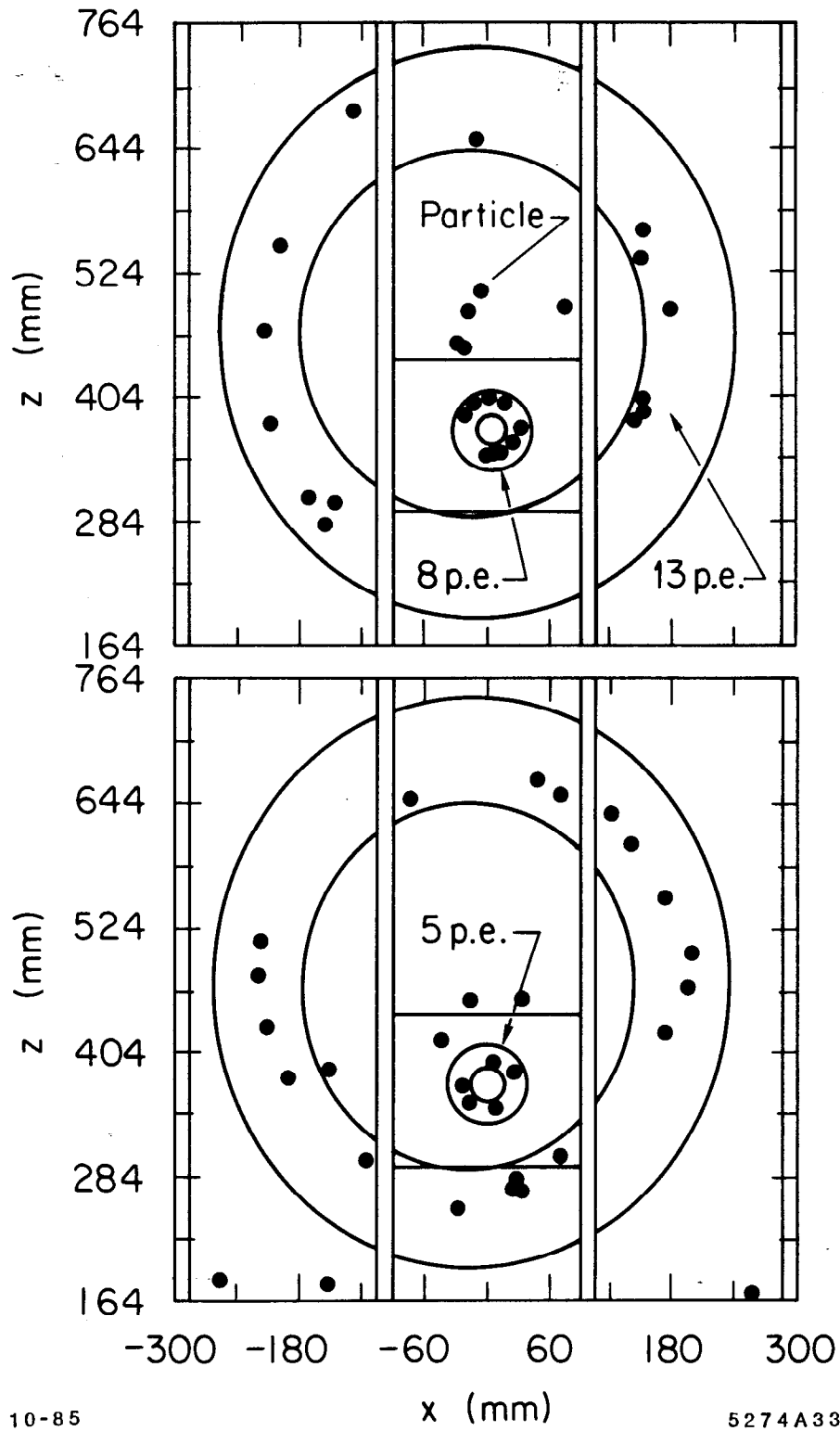


Fig. 23

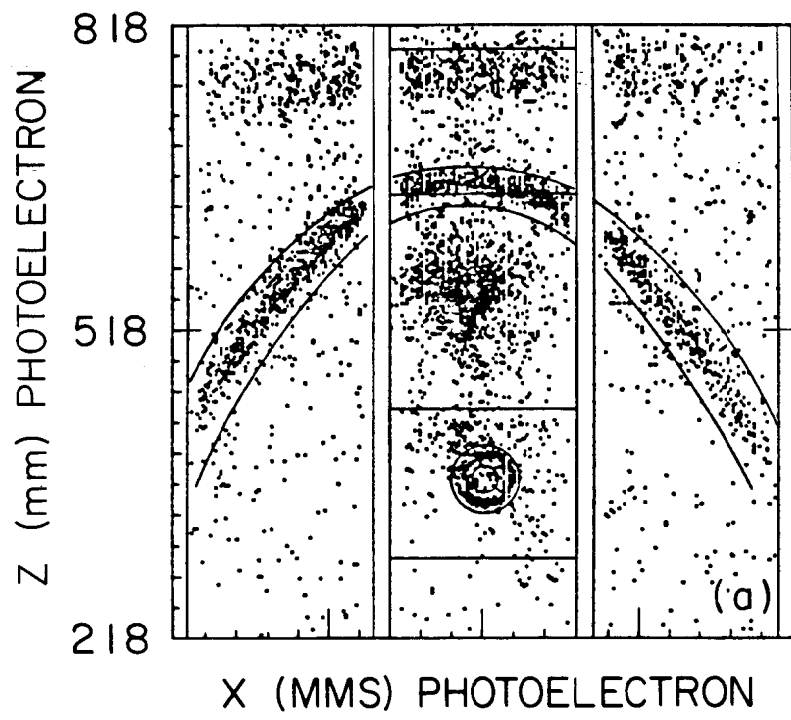


10-85

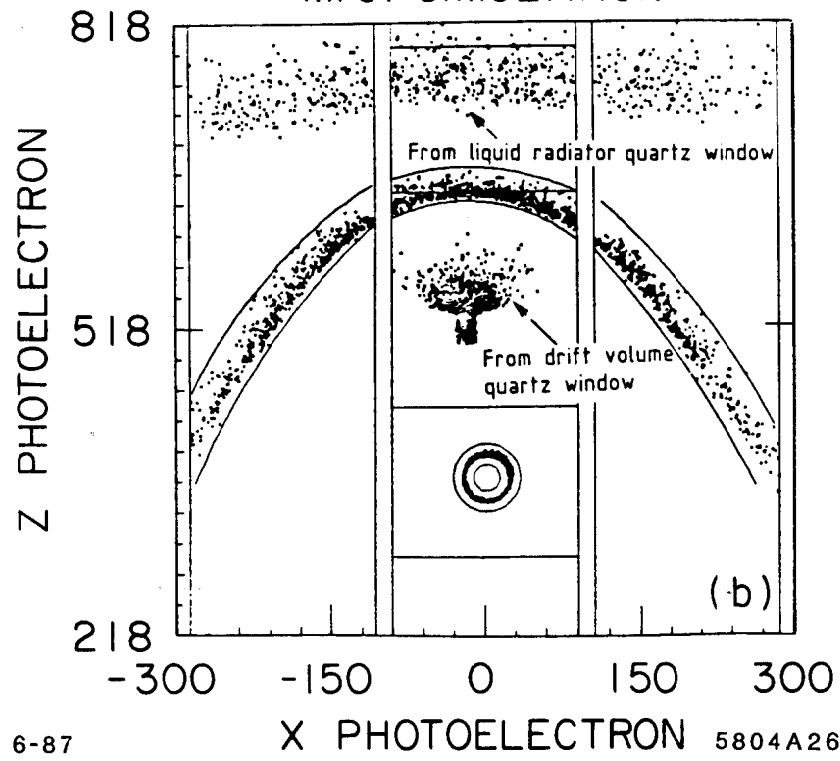
5274A33

Fig. 24





M. C. SIMULATION



6-87

5804A26

Fig. 25

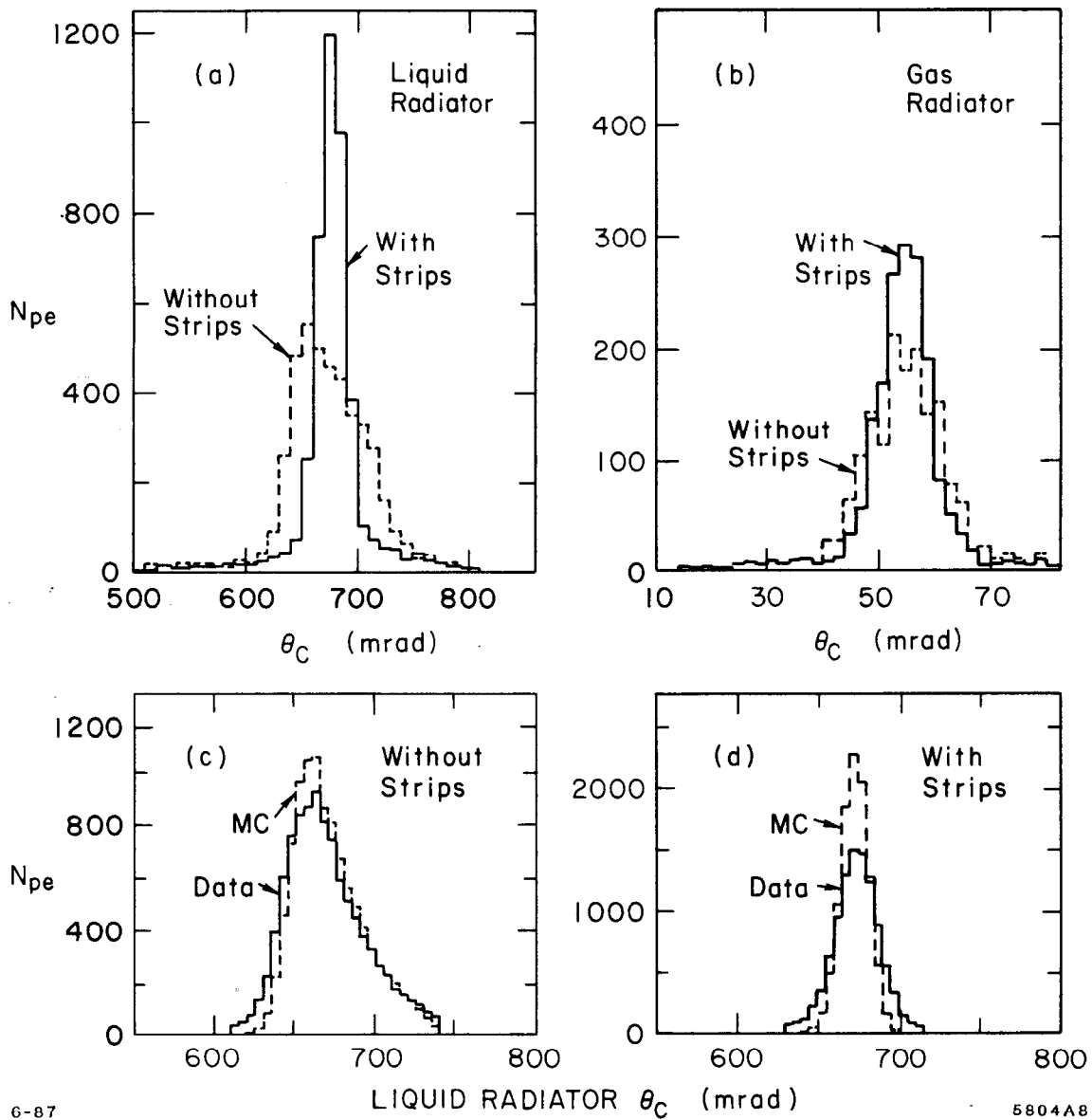


Fig. 26

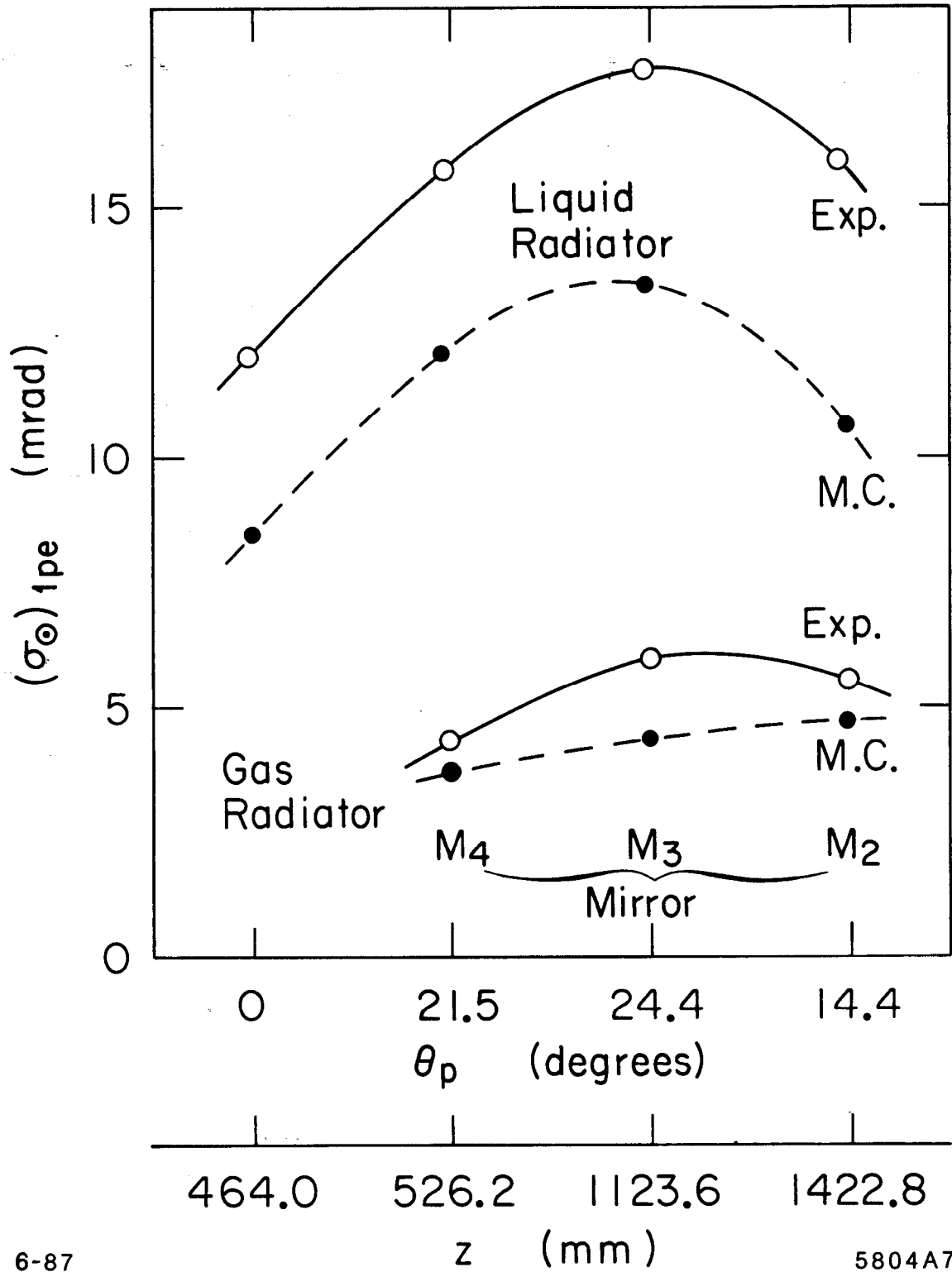
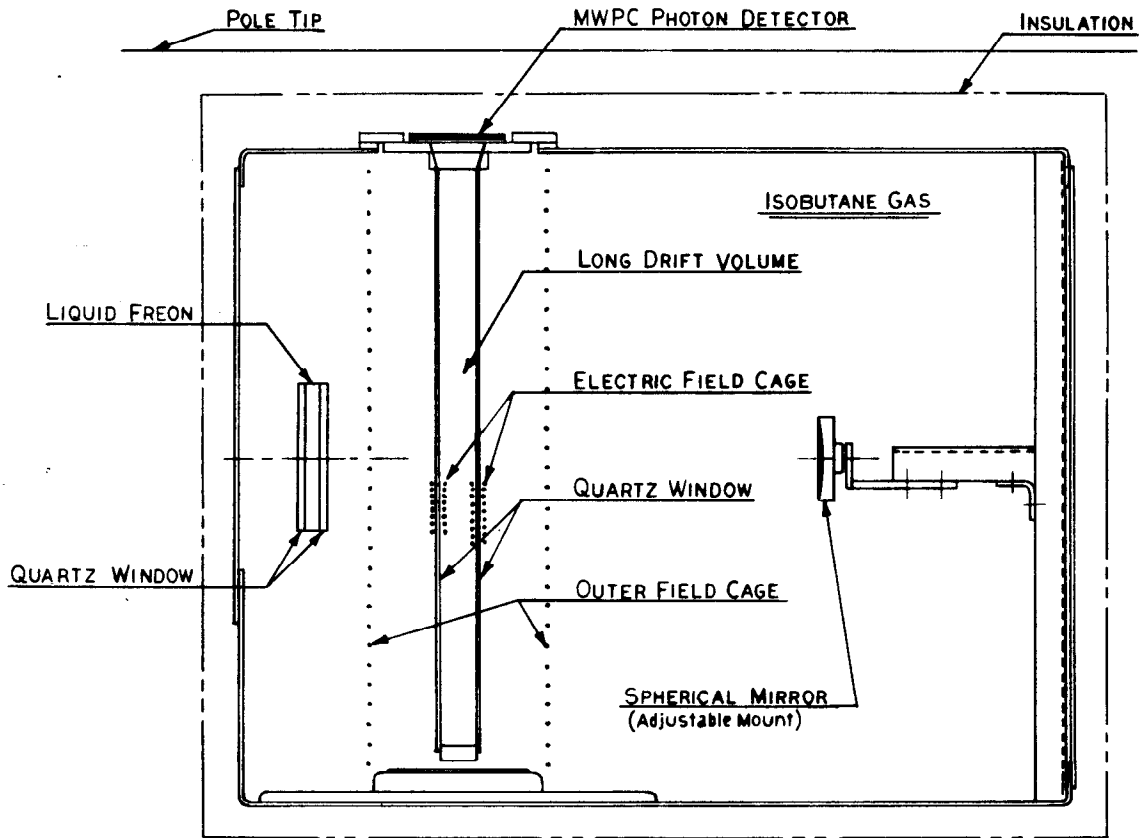


Fig. 27



4-84  
4742A128

Fig. 28

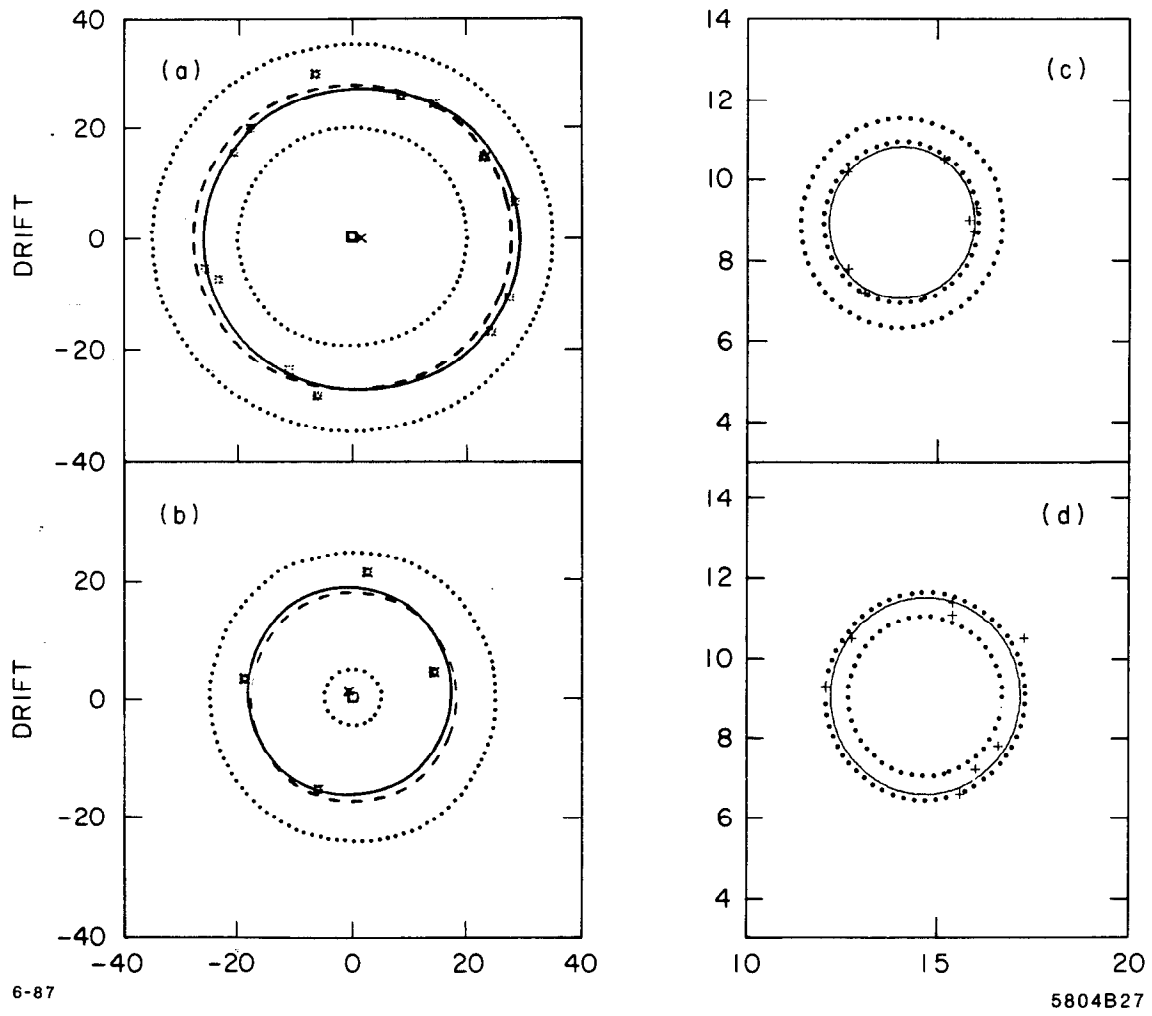
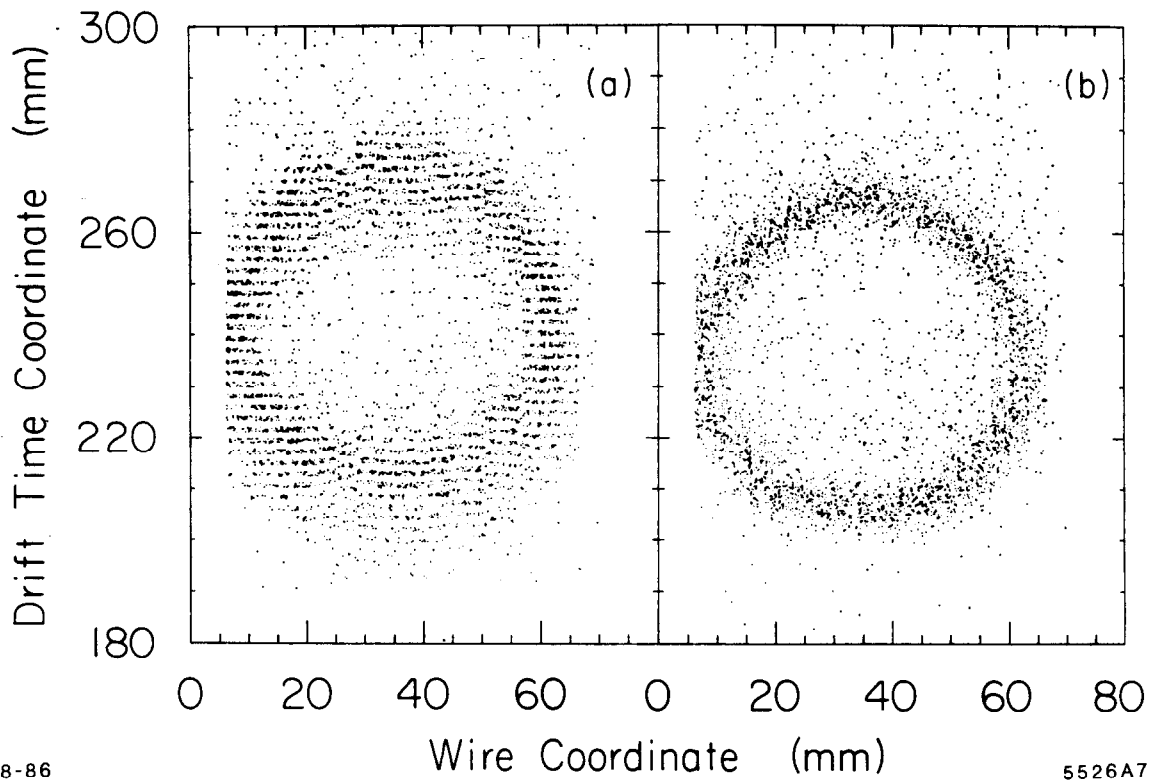


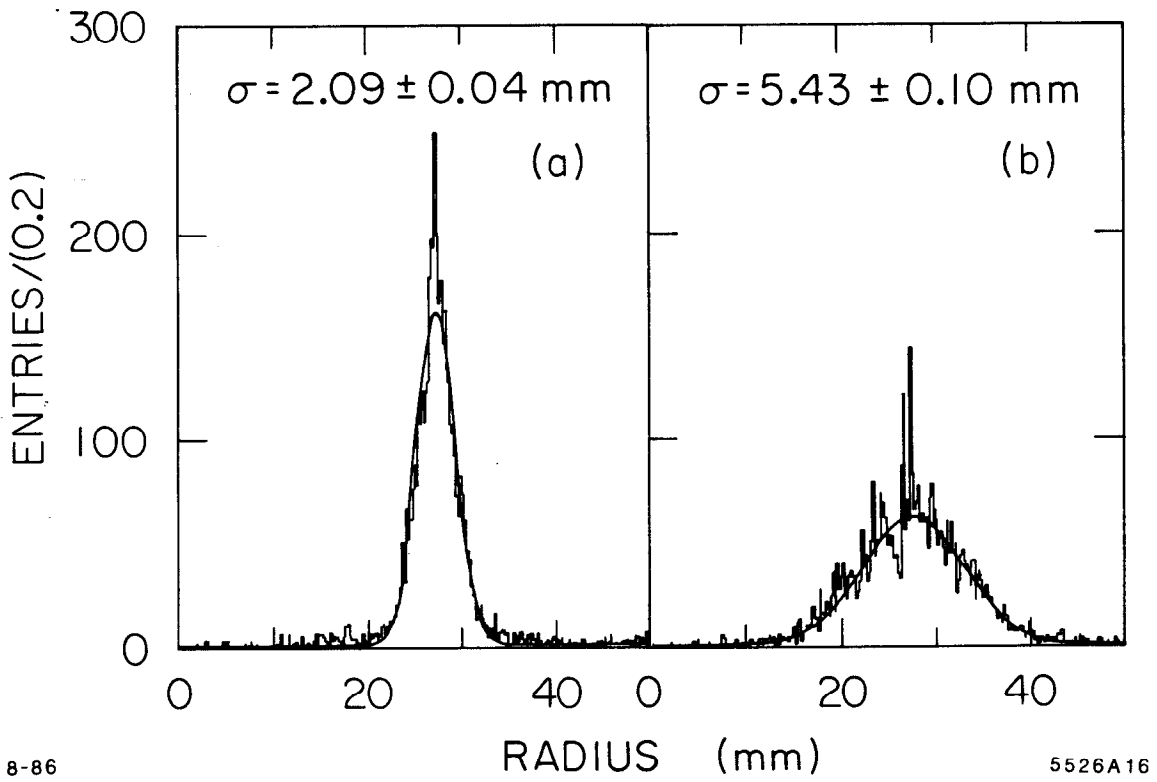
Fig. 29



8-86

5526A7

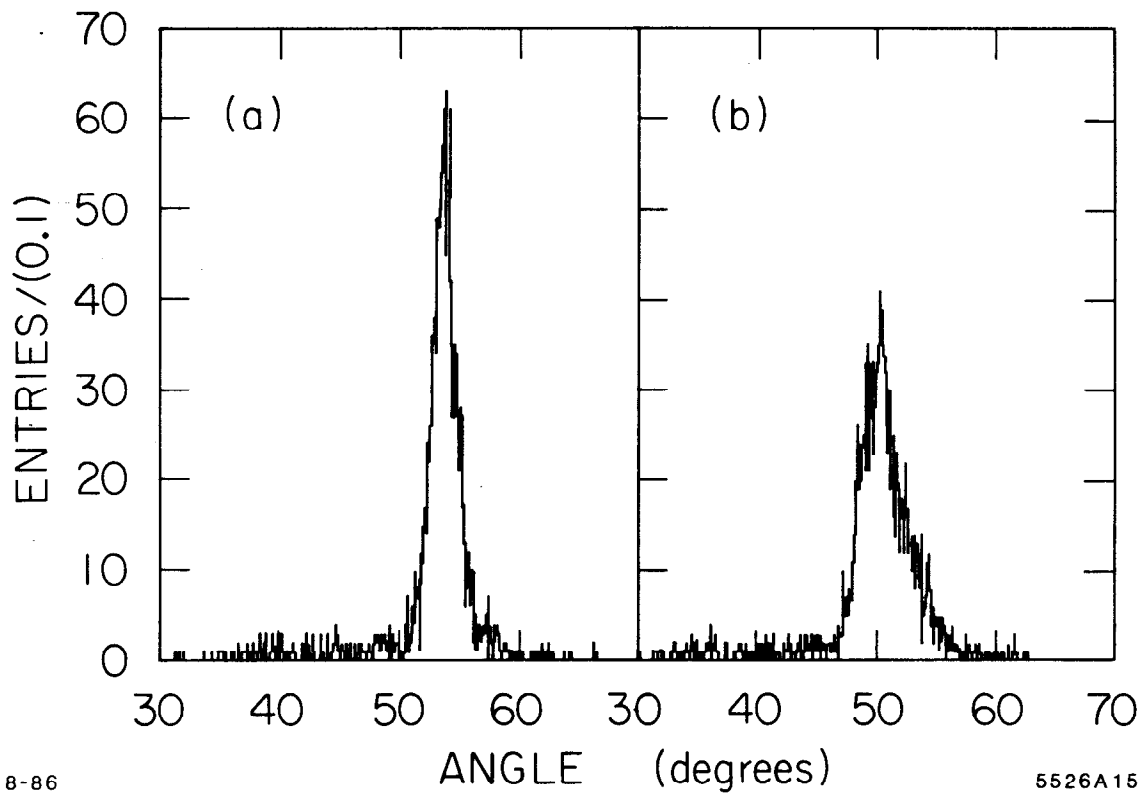
Fig. 30



8-86

5526A16

Fig. 31

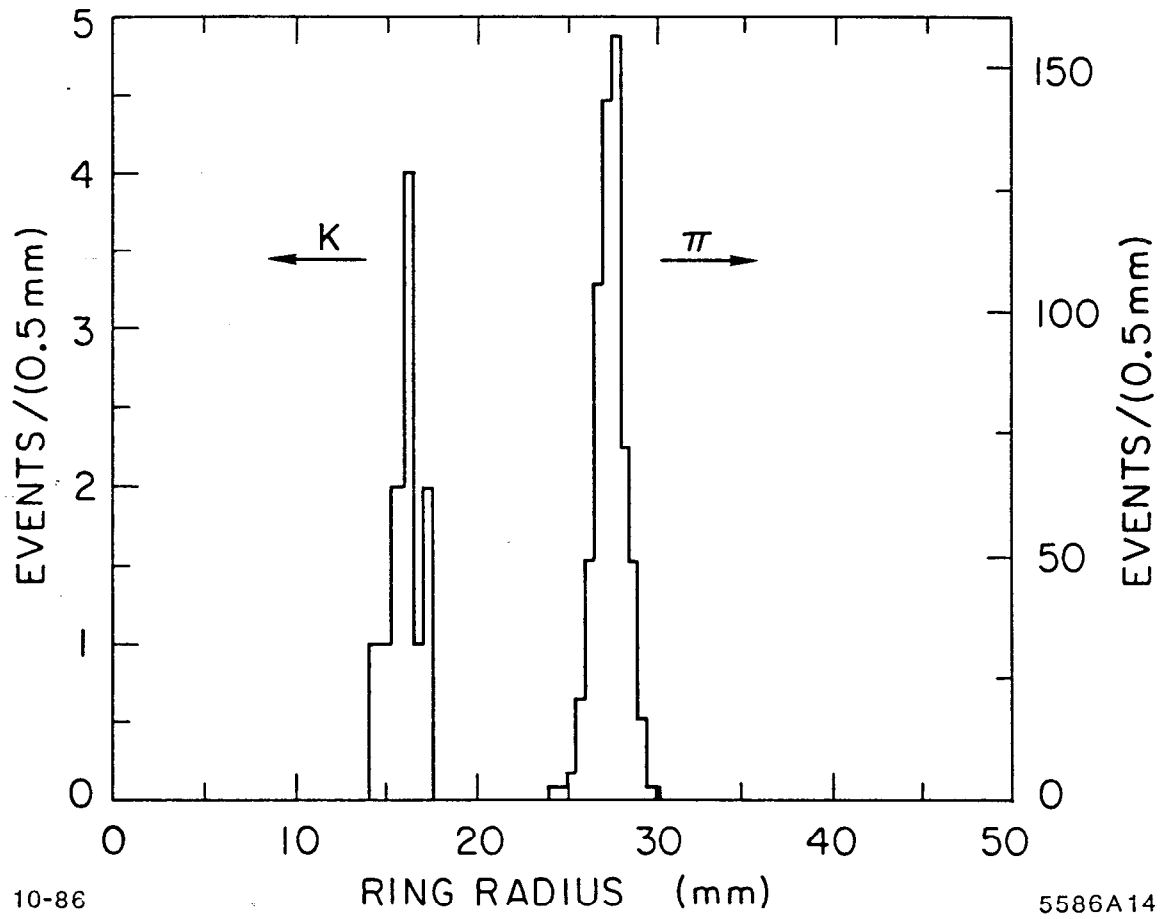


8-86

5526A15

Fig. 32





10-86

5586A14

Fig. 33